August 2023

Investigating the Phytotoxic Impacts of Next-Generation Lithiated Cobalt Oxide Nanomaterials

Eric D. Ostovich
University of Wisconsin-Milwaukee

Recommended Citation

Ostovich, Eric D., "Investigating the Phytotoxic Impacts of Next-Generation Lithiated Cobalt Oxide Nanomaterials" (2023). *Theses and Dissertations*. 3314.
https://dc.uwm.edu/etd/3314

INVESTIGATING THE PHYTOTOXIC IMPACTS OF NEXT-GENERATION LITHIATED COBALT OXIDE NANOMATERIALS

by

Eric Ostovich

A Dissertation Submitted in
Partial Fulfillment of the
Requirements for the Degree of

Doctor of Philosophy
in Freshwater Sciences

at

The University of Wisconsin-Milwaukee
August 2023

ABSTRACT

INVESTIGATING THE PHYTOTOXIC IMPACTS OF NEXT-GENERATION LITHIATED COBALT OXIDE NANOMATERIALS

by

Eric Ostovich

The University of Wisconsin-Milwaukee, 2023
Under the Supervision of Professor Rebecca Klaper

Lithium cobalt oxide nanosheets (LCO) are a type of next-generation transition metal oxide (TMO) nanomaterial and are one of the most commonly used cathode materials utilized in Li-ion batteries (LIB's). With rapidly growing popularity of LIB's as an energy storage technology, many consumer electronics and high-end electric vehicles have begun to incorporate these LIB's into their design. And thus, the manufacturing rate of this nanomaterial has also skyrocketed to levels of environmental significance. However, despite its high levels of production, there is still little means for proper disposal of this nanomaterial, thus resulting in a highly probable environmental release. As LCO is a newer emerging contaminant of concern, we have only begun to study its potential environmental impacts. Recent studies have identified LCO as causing toxicity to eukaryotic organisms like *Daphnia magna*, *Chironomus riparius*, and *Oncorhynchus mykiss*, spanning a few trophic levels. However, there has yet to be any studies addressing the potential toxicity experienced by plant-type organisms. Thus, there is a major gap in our knowledge as to how LCO may impact ecological systems at the primary producing level, which is crucial for the proper structure and function of ecosystems. Additionally, we also have no data to suggest how environmental processes like photosynthesis will be impacted.

This thesis addresses the phytotoxic impacts of LCO to *Raphidocelis subcapitata*, a freshwater microalga and model organism for environmental toxicology. In this work, different endpoints associated with physiological fitness, cellular phenotypes, and molecular interactions are investigated. Additionally, in order to predict the mechanism of action (MoA) through which LCO perturbs *R. subcapitata*, novel high-throughput phenotypic profiling (HTPP) methods were developed specifically for algal cells that employ multiplexed fluorescence cytochemistry coupled with high-content imaging (HCI). These HTPP methods were used to compare changes in the complex phenotypes of LCO-treated cells to that of compounds with known MoAs as a means to predict the phytotoxic MoA of LCO. The results of these investigations demonstrate impaired growth and net carbon biomass assimilation as physiological consequences of LCO exposure, while triggering an increase in chlorophyll and neutral lipid content. Furthermore, enhanced darkfield hyperspectral imaging revealed deposits of internalized LCO nanoparticles, thus suggesting the potential for LCO to directly interact with key subcellular components of *R. subcapitata*, as opposed to simply adhering to/covering the surface of the cells. Lastly, HTPP analyses revealed electron transport inhibition as the major phytotoxic MoA of LCO and demonstrated the irreversible oxidation of photosystem II (PSII) proteins, which are responsible for catalyzing the initial reaction of photosynthesis. Overall, these findings expand the mechanistic knowledge of LCO toxicity to plant-type organisms and the methods described in this work provide a novel framework for investigating chemical interactions within phycological entities.

To
my family,
friends,
and mentors,
who have all made an impact on my life and career,
and helped to make this journey a possibility for me.

TABLE OF CONTENTS

LIST OF FIGURES

LIST OF TABLES

ACKNOWLEDGEMENTS

Firstly, I’d like to express the sincerest of gratitude to my mentor, Dr. Rebecca Klaper. I could not have asked for a better person to lead me on this journey, and her guidance has truly helped to make me a better scientist. Additionally, thanks also to all the members of the Klaper lab who helped to make these last several years a joy to come to work. I would like to thank the NSF Center for Sustainable Nanotechnology, who’s financial and professional support made all of the work in this thesis possible. Also, a special thanks to Angela Schmoldt and Timothy Wahl, at the School of Freshwater Science, who’s expertise aided in the success of this experimental work.

Next, I would like to thank all of my committee members whose input helped to improve the quality of this work: Dr. Harvey Bootsma, Dr. Laodong Guo, and Dr. Jason White.

Finally, I would like to thank all of my family for their love and support over the years, in all things academic, and in life. Without their encouragement and belief in myself, none of my successes would be possible.

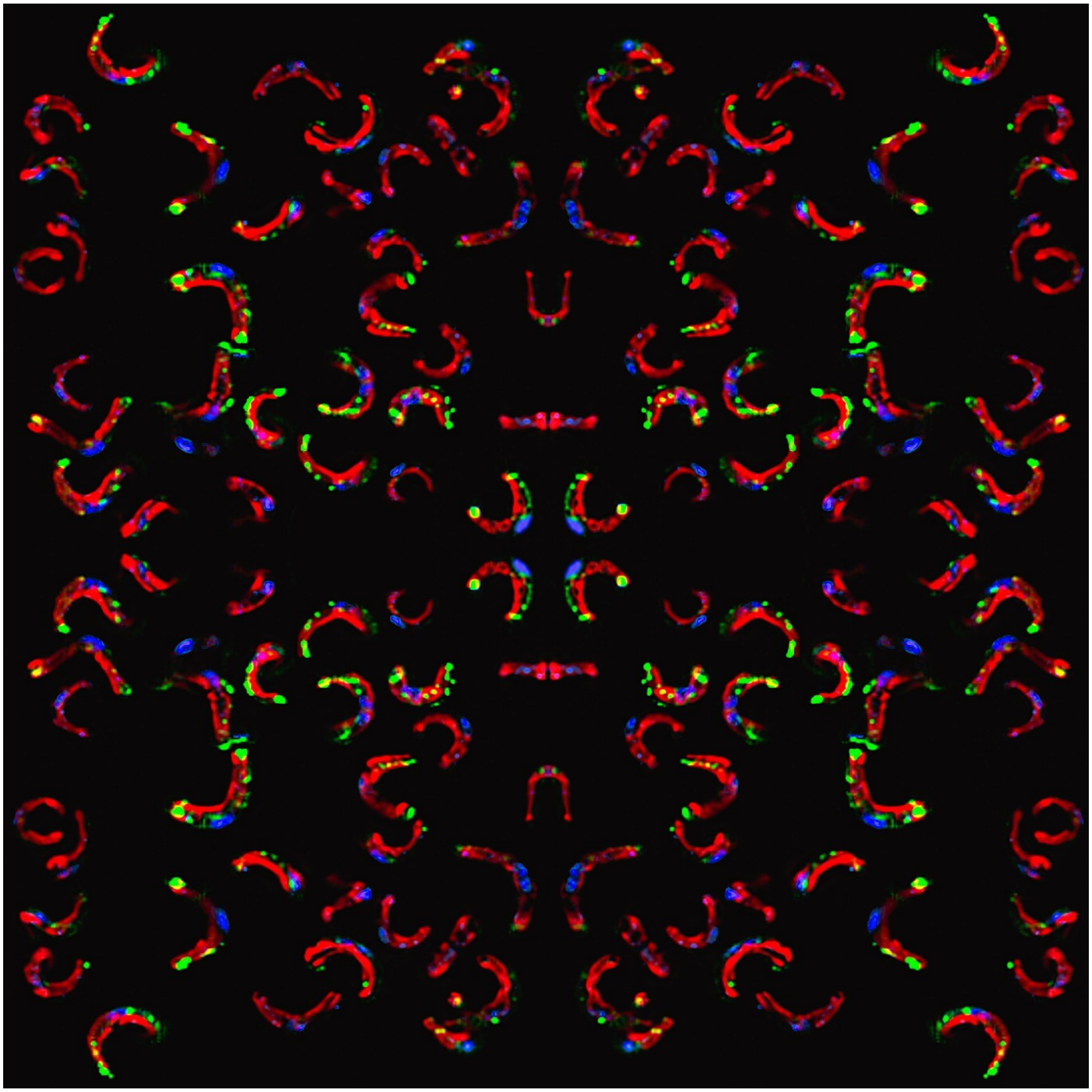

Introduction

LiCoO$_2$ (LCO) is a type of rhombohedral shaped, transition metal oxide (TMO) material with intercalating layers of Li and CoO$_2$.[1] This material was originally introduced by J. B. Goodenough in 1982 as a new cathode material for high energy density batteries,[2] and has since become the most commonly used cathode material in rechargeable Li-ion batteries (LIB).[1] LCO is very attractive as a cathode material because of its desirable characteristics such as a having a high theoretical specific capacity, high theoretical volumetric capacity, low self-discharge, high discharge voltage, and good cycling performance.[3] In recent years, however, nanoscale LCO has become preferred over its bulk counterpart due to its enhanced battery rate performance. This is because at the nanoscale, LCO has the advantage of having shorter Li-ion diffusion lengths compared to micron-sized particles, in which only ~50% of Li-ions can be used, thus improving the overall electronic transport.[1,3]

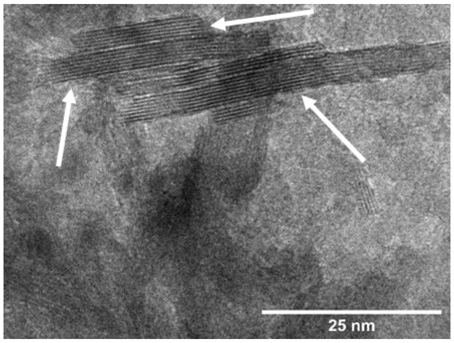

Figure 1: Transmission electron microscopy (TEM) Image of LCO.

Since LCO is one of the most popular battery cathode materials, it has been incorporated into many types of consumer electronics from cell phones and laptops to high-end electric vehicles. Furthermore, in efforts to improve battery life of LIB's as we become more dependent on this technology, increasing amounts of this nanomaterial are continually added to newer battery packs as energy storage capacity is directly proportional to the mass of the battery material used [4]. Both situations translate to LCO's manufacturing rates rising to levels of environmental significance/concern. Specifically, in 2015, LCO was being produced at an annual rate of 79,000 metric tons, which increased to an estimated annual rate of ~200,000 tons in 2020, and is projected to increase to an annual rate of ~380,000 tons by 2025.[4] To put this into perspective, this means that by 2025, we will be producing more of this specific type of next-generation TMO nanomaterial yearly than the combined production of all other first generation TMO nanomaterials (TiO_2, ZnO, SiO_2, etc.) in the year 2010 (~318,100 tons).[5] What makes this matter particularly concerning, however, is that there is little to no infrastructure for recycling or for properly disposing of LIB's, nor is there any economic incentive to do so as it's cheaper to just manufacture new materials.[4] For example, it's currently estimated that less than 5% of all LIB's are being recycled, with the rest ending up in landfills or being disposed of in other mean of un-sustainable storage.[6] As such, this means that there is a high probability for LCO to be unintentionally released into the environment, thus posing an ecological risk. And what exacerbates this risk is that LCO contains high-valence metals with unique catalytic properties, high reactivity, and have known inherent toxicity.[3,7] Thus, an important challenge we currently face is in understanding the environmental impacts that LCO has to a wide diversity of organisms in the environment.

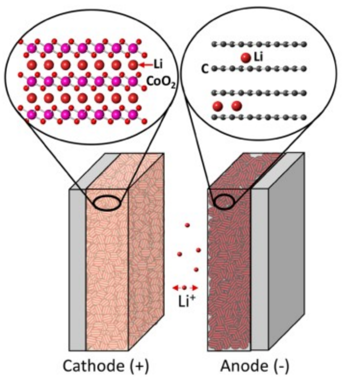

Figure 2: Illustration of Li^+ movement in LIB at nanoscale, adapted from Hamers, 2020.

Recent studies have begun to evaluate the general toxicological impacts of LCO exposure. For example, in daphnids, LCO has been found to reduce survival, rates of reproduction, and induce a differential expression in stress related genes;[8] in rainbow trout gill cells, LCO has been seen to impact cell viability and cause significant production of reactive oxygen species (ROS);[9] and in chironomids, LCO has been reported to cause delays in growth and development, as well as hinder the process of heme synthesis.[10] However, more interestingly, LCO has also been reported to cause a number of molecular-level impacts. For example, in daphnids, there have been reports of an overwhelming disruption to energy metabolism related genes;[11] in rainbow trout gill cells, there have been similar reports of significant overrepresentation in energy metabolism related pathways;[12] and in chironomids, LCO has been reported to participate in redox reactions and alter the redox state of and Fe-S proteins, which are important for electron transfer, especially in energy metabolism related pathways.[13] These results are interesting because, at the molecular level, all three of these organisms are showing signs of impaired energy metabolism, and the significance of seeing this exact impairment in multiple organisms suggests that electron transport inhibition and energy starvation may be a unifying molecular level impact of LCO exposure across species. However, there are still many gaps in our knowledge that speak to the entirety of LCO's environmental consequences. Firstly, there has yet to be any data on the general toxicological impacts of plant-type species, whose crucial role in sustaining ecosystem health includes driving nutrient cycles and energy flow. Secondly, while we have some data to suggest that LCO interferes with pathways like glycolysis and respiration in animal-type eukaryotic organisms, we have no understanding as to how LCO may impact other pathways in plant-type organisms that are also tied to environmental processes, like photosynthesis. Thirdly, given an exposure of LCO to plant-type organisms, we have no data that extrapolate the molecular level interactions between the two, nor confirm any unifying molecular mechanisms of toxicity across plant-type and animal-type eukaryotic organisms. One model organisms that could potentially help fill in these knowledge gaps is *Raphidocelis subcapitata*.

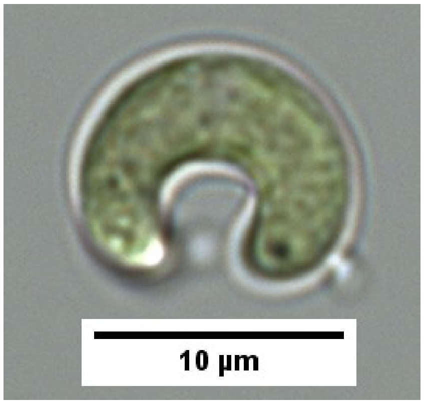

Figure 3: Unicellular microalgae, *Raphidocelis subcapitata*.

R. subcapitata is a prevalent type of green microalgae found in freshwater ecosystems that, as a primary producer, is important for the overall health and sustainability of freshwater ecosystems. In terms of phytotoxicology, *R. subcapitata* is an excellent model organism to use as this particular organism happens to be an EPA established model for ecotoxicology[14] and has been widely used as a bioindicator species for toxicological risk assessment studies. Furthermore, *R. subcapitata* is suitable for these studies due to its many desirable characteristics. For one, it has a high sensitivity to various contaminants (especially metals), making it a good bioindicator species in detecting toxicological impacts at low quantities. As such, it is considered a particularly important organism in studies pertaining to water quality and environmental assessments. Additionally, *R. subcapitata* has an exponentially high reproduction efficiency which allows large quantities of it to be grown in relatively short periods of time, thus making it a good organism to use when setting up large scale exposures with various treatments and multiple replicates. Lastly, this organism has good experimental reproducibility, which is ideal for the design of experiments with a high degree of reliability.

Chapter 1.

Physiological Impacts of *Raphidocelis subcapitata* in Response to Lithiated Cobalt Oxide Nanomaterials

1.1. Abstract

Complex metal oxide nanomaterials, like $LiCoO_2$ (LCO) nanosheets, are among the most widespread classes of nanomaterials on the market. Their ubiquitous application in battery storage technology drives their production to rates of environmental significance without sufficient infrastructure for proper disposal/recycling, thus posing a risk to ecosystem health and sustainability. This chapter assesses the general toxicological impacts of LCO when exposed to *Raphidocelis subcapitata*; physiological endpoints relating to growth and energy production are considered. Algal growth inhibition was significantly increased at concentrations as low as 0.1 $\mu g \cdot mL^{-1}$, while exhibiting an EC_{50} of 0.057 $\mu g \cdot mL^{-1}$. The average biovolume of cells were significantly enlarged at 0.01 $\mu g \cdot mL^{-1}$, thus indicating increased instances of cell cycle arrest in LCO-treated cells. Additionally, LCO-treated cells produced significantly less carbon biomass while significantly overproducing neutral lipid content starting at 0.1 $\mu g \cdot mL^{-1}$, thus indicating interference with CO_2 assimilation chemistry and/or carbon partitioning. However, the relative abundance of chlorophyll was significantly increased, likely to maximize light harvesting and compensate for photosynthetic interference. Cells that were treated with dissolved Li^+/Co^{2+} ions did not significantly impact any of the endpoints tested, suggesting LCO phytotoxicity is mainly induced through nano-specific mechanisms rather than ion-specific. These results indicate that this type of nanomaterial can significantly impact the way this algae proliferates, as well as the way it produces and stores its energy, even at lower, sublethal, concentrations. Furthermore, impairments to crucial cellular pathways, like carbon assimilation, could potentially cause implications at the

ecosystem level. Thus, in future work, it will be important to characterize the molecular mechanisms of LCO at the nano-bio interface.

1.2. Introduction

As the field of nanotechnology continues to grow, and more consumer products start to incorporate nanomaterials into their design, understanding the environmental impacts of these nanomaterials is increasingly important. $LiCoO_2$ (LCO), for example, is a type of complex metal oxide nanosheet used as a cathode material for lithium ion batteries,[7] which is found in many consumer electronics and high-end vehicles.[3] Increasing manufacturing rates, as well as a lack of infrastructure and economic incentive for recycling/disposal[4,15] make LCO an emerging contaminant of concern. Since LCO contains high valence metals with unique catalytic properties, high reactivity, and known inherent toxicity, an accidental exposure of this type of nanomaterial could lead to many adverse outcomes.

Recent studies have begun to evaluate the general toxicological impacts of LCO exposure. For example, in *D. magna*, LCO has been found to reduce survival, rates of reproduction, and induce a differential expression in stress related genes;[8] in RTgill-W1 cells, LCO has been seen to impact cell viability and cause significant production of ROS;[9] and in *C. riparius*, LCO has been reported to cause delays in growth and development, as well as hinder the process of heme synthesis.[10] However, more interestingly, LCO has also been reported to cause a number of molecular-level impacts. For example, in *D. magna*, there have been reports of an overwhelming disruption to energy metabolism related genes;[11] in RTgill-W1 cells, there have been similar reports of significant overrepresentation in energy metabolism related pathways;[12] and in *C. riparius*, LCO has been reported to participate in redox reactions and alter the redox state of and Fe-S proteins, which are important for electron transfer, especially in energy metabolism related pathways.[13] These findings are interesting because, at the molecular level, all three of these organisms are showing signs of impaired energy metabolism, and the significance of seeing this exact impairment in multiple organisms suggests that disruptions to energy related pathways may be a unifying molecular level impact of LCO across species. However, there are still many gaps in our knowledge as to the entirety of LCO's environmental consequences. Firstly, there has yet to be any data on the general toxicological impacts of algal species, whose crucial role in sustaining ecosystem health includes driving nutrient cycles and energy flow.[16] Secondly, while we have some data to suggest that LCO interferes with pathways like glycolysis and respiration in animal-type organisms, we have no understanding as to how LCO may impact other pathways in primary producing-type organisms that are also tied to environmental processes, like photosynthesis.

The assimilation of CO_2, by primary producers, is necessary to support all life on Earth as consumers in the environment rely on this net primary production of carbon biomass as a source of chemical energy. More specifically, phytoplankton account for about half of the total global primary productivity with marine phytoplankton fixing around 50000 Tg CO_2 annually,[17] and freshwater phytoplankton fixing around an estimated 133 Tg CO_2 annually.[18] As such, a decrease in the efficiency of phytoplankton primary productivity could consequentially alter ecosystem energy budgets.

In this chapter, *Raphidocelis subcapitata,* a model algal bioindicator species,[14] was exposed to LCO for 48 hours. Several physiological endpoints were recorded in order to assess several aspects of cell fitness. Given our current understanding of the toxicological and molecular level impacts of LCO in other organisms, we hypothesize that LCO may negatively impact facets of algal physiology related to growth and energy production.

1.3. Materials and Methods

LCO Synthesis and Characterization.

Sheet-like nanoparticles of Li_xCoO_2 were synthesized using the techniques described in previous studies.[19,20] Water with a resistivity 18.2 $M\Omega\cdot cm^{-1}$ was used for each step during the synthesis. A ($Co(OH)_2$) precursor was prepared using a precipitation reaction between LiOH and $Co(NO_3)_2\cdot 6H_2O$. A 1 M $Co(NO_3)_2\cdot 6H_2O$ was added drop-by-drop to a 0.1 M solution of LiOH. The precipitate was isolated and washed with 3 repeated cycles of centrifugation for 5 min at 4696 g as to isolate a pellet of particles, that was then resuspended in water. Next, the supernatant was removed after washing and the solid product was dried in a vacuum oven at 30 °C overnight. The $Co(OH)_2$ precursor was then lithiated to form Li_xCoO_2 by adding 0.20 g $Co(OH)_2$ particles to a molten salt flux of 6:4 molar ratio of $LiNO_3$:LiOH at 200 °C in a PTFE container equipped with magnetic stirring in a silicone oil bath. The particles were then heated and stirred in this molten salt flux for 30 min and the reaction was quenched with water. The precipitate was isolated and washed by 3 repeated cycles of centrifugation for 5 min at 4696 g to isolate a pellet of particles, which were then resuspended in water. Then the product was isolated from the supernatant and dried in a vacuum oven at 30 °C overnight.

The particles, digested in aqua regia, were analyzed using inductively coupled plasma – optical emission spectroscopy (ICP-OES) to yield a Li:Co ratio of 0.92:1. Surface area measurements, determined by nitrogen physisorption, yielded a surface area value of 125 $m^2\cdot g^{-1}$. Powder X-Ray Diffraction yielded patterns consistent with previously published work which could be indexed to the $R\bar{3}m$ space group (found in **supplementary information**). Individual LCO particles were imaged and sized using a FEI Tecnai T12 transition electron microscope where only particles completely captured in the image were measured. Thickness was measured of particles that appeared very dark as this means they were viewed edge-on. Length of particles were measured if clearly defined endpoints were visible and if it could reasonably be assumed that it was a single particle as opposed to an aggregate. Dynamic light scattering (DLS) and zeta potential measurements of LCO suspensions in algae media (found in **supplementary information**) were obtained with a Zetasizer Nano ZS Size Analyzer from Malvern Panalytical.

Algal Cell Culture.

A stock culture of *R. subcapitata* was inoculated at 1×10^5 Cells·mL^{-1}, was cultured in a complete media comprised of Bold Modified Basal Medium (Sigma, B5282) and 18 MΩ water. Cells were illuminated with a full spectrum T8 light bulb at a continuous timescale. The stock solution was aerated with an aquarium air pump.

Exposure Setup.

This exposure was done to assess the impacts of LCO on *R. subcapitata* after 48 hours of exposure. Algae were exposed to one of four LCO concentrations or untreated control (0 μg·mL^{-1}, 0.01 μg·mL^{-1}, 0.1 μg·mL^{-1}, 1 μg·mL^{-1}, & 10 μg·mL^{-1} LCO), an ion control that contained the concentration of lithium and cobalt ions that would be present in the algae media containing 10 μg·mL^{-1} of LCO after 48 hours, and a dark control that was deprived of any light. In each treatment, done in quadruplicates, cells were seeded from the stock culture, after cells were growing exponentially, at 7×10^5 cells·mL^{-1} in T-25 flasks. A stock suspension of LCO was constituted in the algal complete media at 100 μg·mL^{-1}. This suspension was sonicated for 25 minutes before the addition to respective samples to break up any aggregated nanoparticles. Additionally, an ion solution made from LiOH and $CoCl_2\cdot H_2O$, also constituted in complete media, was made at 10X the concentration of ion dissolution of 10 μg·mL^{-1} of LCO after 48 hours.

Dissolution of these particles was previously assessed using ICP-MS, where Li^+ was found to have a dissolution of 1024 $\mu g \cdot L^{-1}$ and Co^{2+} 239 $\mu g \cdot L^{-1}$.[10] For each treatment, complete media, LCO suspension, or 10X ion solution was added to 45 mL of cell suspension at a final volume of 50 mL. The samples were placed under full spectrum illumination at a photon flux of 70 $\mu E \cdot m^{-2} \cdot s^{-1}$, with the exception of the dark control samples, which were deprived of any light. At the conclusion of the exposure, the algal cells were spun down at 12000 x g for 7 minutes, and the media was aspirated. An additional vacuum centrifugation step was done to remove all moisture from the algae cell pellets that were used for elemental analysis.

Growth Inhibition.

Growth inhibition was measured as a first-line indicator of a toxicological response, as well as to determine the sensitivity of the algal cells to LCO.[21] Before pelleting the algae samples, the cell concentration in each sample was determined by using optical density (OD) with an Agilent BioTek Synergy H4 Hybrid Microplate Reader at λ=680 nm. An OD_{680} was used since this microalgae absorbs light best at this wavelength. The absorptivity coefficient (found in **supplementary information**) was determined by plotting known concentrations of algae, determined with hemocytometry, against their respective absorbances. A 109 µL aliquot of each cell sample was placed in a well of a glass bottom 384 well plate (Cellvis, P384W-1.5H-N), which had a liquid height of 1 cm. Control samples were blanked with a solution of algae media while treated samples were blanked with an associated nanoparticle/ion control in order to account for the amount of light absorbance/scattering caused by the presence of LCO/ions in the medium. These nanoparticle/ion controls consisted of a suspension of LCO/Li^+ & Co^{2+} ions constituted in algae media that emulated the respective concentration of LCO/ions present in each treatment. Cell concentration values at T_0 and T_{48} were used to calculate growth rates and growth inhibition per OECD guidelines [21] as seen below, respectively:

$$\mu_{i-j} = \frac{\ln X_j - \ln X_i}{t_j - t_i} \ (day^{-1}) \ \ldots\ldots\ldots\ldots\ldots\ldots\ldots\ldots\ldots\ldots\ldots\ldots (1)$$

where μ_{i-j} represents the is the average specific growth rate from time i to j, X_i is the cell concentration at time i, and X_j is the cell concentration at time j;

$$\%I_r = \frac{\mu_C - \mu_T}{\mu_C} \times 100 \ \ldots\ldots\ldots\ldots\ldots\ldots\ldots\ldots\ldots\ldots\ldots\ldots (2)$$

where $\%I_r$ represents the percent inhibition in average specific growth rate, μ_C is the mean value for average specific growth rate (μ) in the control group, and μ_T is the average specific growth rate for the treatment replicate. An EC_{50} value, based on the growth inhibition data, was statistically determined with a three-parameter log-logistic model using the drc package in R.[22]

Biovolume.

Biovolume, which can be described as the volumetric space occupied by an algal cell, is a morphological trait that was used as a simple measurement of phenotypic change to the cell. Alterations to the biovolume of microalgae can have an impact on its functional properties like access to nutrients and light, velocity of sinking, and tolerance to grazing,[23] however, in the case of *R. subcapitata*, it can also be an indication of disruption to cell cycle progression.[24] Cell samples from each treatment were imaged with an EVOS™ XL Core Imaging System, equipped with an EVOS™ 40X LWD achromatic phase contrast objective. Cell images were processed in ImageJ to estimate single cell dimensions using methods described by.[25] Biovolumes of individual algal cells were calculated as described by[26] with the assumption that *R. subcapitata* is generally shaped like a sickle-shaped cylinder[27] per the following equation:

$$V = \frac{\pi}{6} \cdot l \cdot w^2 \ldots\ldots\ldots\ldots\ldots\ldots\ldots\ldots \text{(3)}$$

where V represents the biovolume of the cell, l is the length of the cell, and w is the transapical width of the cell. At least 100 cells were analyzed from each independent sample and were averaged, and then the average values for all independent samples were averaged by treatment to obtain the average biovolume value.

Elemental Analysis.

Dried algae pellet samples were accurately weighed into small tin cups on a microbalance. Sample filled tin cups were crushed into small spheres that could be inserted into the elemental analyzer's (EA) auto sampler. Samples dropped, one at a time, from the rotating auto sampler into the combustion column where they were converted into simple gases (e.g. CO_2, H_2, N_2). Unwanted materials such as halogens, sulfur, phosphorus, NOx, and excess oxygen from combustion were removed with Cu, CrO_3, CoO, $Mg(Cl_4)_2$, and NaOH reagents in the oxidation/reduction chamber. From there, elements were separated by gas chromatography (GC) with a helium carrier gas before passing by a thermal conductivity detector.

Post run analyses started by investigating the retention time (RT) of each sample. The RT is the amount of time in decimal minutes between sample injection and chromatogram peak. Because the EA uses GC, the RT is directly related to the molecular weight (MW) of the simple gas, which in this case was used to estimate the amount of carbon present in each algae sample. Acetanilide standards were used to construct a calibration curve.

Net production of Carbon Biomass.

The total amount of carbon in each sample was calculated using the carbon peak areas measured by the EA and in reference to the acetanilide standard curve. Then the amount of carbon per cell was calculated by dividing the amount carbon in the sample by the number of cells from the pellets present in each respective sample. The net production of carbon biomass per cell for each sample was then calculated using the following equation:

$$NCP = \left(\frac{Mass\ C_{Sample}}{\#cells_{Sample}}\right) - \bar{x}\left(\frac{Mass\ C_{Dark}}{\#cells_{Dark}}\right) \text{ ……………..…..…………(4)}$$

Where NCP represents net carbon biomass produced per cell, $Mass\ C_{Sample}$ is the mass of carbon in any given sample, $\#cells_{Sample}$ represents the number of cells in any given sample determined through OD, $Mass\ C_{Dark}$ is the mass of carbon specifically in the dark controls, and $\#cells_{Dark}$ is the number of cells specifically in the dark controls. The mass of carbon per cell for each sample was subtracted by the average mass of carbon per cell from the dark controls, as they theoretically should not have produced any carbon biomass without a light source or dissolved organic carbon supplemented in the medium, thus yielding a net production in carbon biomass per cell value for each sample. NCP values were then further normalized to the average biovolume in each sample as a means to correct for changes in cell size.

Neutral Lipid Content.

Neutral lipid content was measured as an additional stress response since these lipid droplets tend to accumulate downstream of certain stressors and/or nutrient depravation in microalgae and can be indicative of impairments to energy metabolism.[28] To assay for neutral lipid content, cells were stained post exposure with BODIPY™ 505/515, which selectively binds to neutral lipids. 1×10^6 cell aliquots were obtained from each sample and transferred to sterile microcentrifuge tubes, where additional algal complete media was added at a final volume of 1 mL. BODIPY™ was then added to each sample at a final concentration of 5 µM, including a no-cell control with only complete media, whereafter samples were incubated in darkness at room temperature for 15 minutes. 100 mL aliquots were transferred to a glass bottom 384 well plate (Cellvis, P384W-1.5H-N) and fluorescence measurements were then taken on an Agilent BioTek Synergy H4 Hybrid Microplate Reader at an excitation and emission wavelength of 470/20 nm and 540/20 nm, respectively. Relative lipid content was calculated by taking the difference of the average no-cell control and respective sample RFU values and then normalizing to the corrected non-treated cell control RFU values. Additionally, cells were also imaged with an EVOS™ M7000 Imaging System to visualize the lipid droplets as a qualitative assessment of neutral lipid content.

Single-Cell Chlorophyll Fluorescence Microscopy.

100 µL aliquots from each sample were plated in to a well of a glass bottom 384 well plate (Cellvis, P384W-1.5H-N) and spun gently at 600RPM for 1 minute to concentrate cells at the bottom of the well. Cells were then dark adapted for 30 min before imaging with an ImageXpress Micro XLS High-Content Screening System. For image acquisition, cells were visualized using a Cy 5 filter (ex/em: 628/692), thereby exciting chlorophyll molecules, and a 60X Plan Fluor 0.85 NA objective (Molecular Devices, 1-6300-0414); 16 sites per well were acquired. For representative cell figures, images were also acquired with a 100X CFI L PLAN EPI CC 0.85 NA objective (Molecular Devices, 1-6300-0419) for better resolution. After acquiring images, bioimage analysis was conducted with CellProfiler [v4.2.1][29] for segmenting images and measuring the respective fluorescence intensities of individual cells. The average "mean_cell_intensity" values from each treatment were used to represent the relative abundance of chlorophyll content.

Enhanced Dark-Field Hyperspectral Imaging.

To confirm cellular uptake of LCO, algal samples were analyzed using the CytoViva Enhanced Darkfield Hyperspectral System, which uses patented darkfield optics to generate high contrast, high signal-to-noise ratio images. These images were scanned via the CytoViva HSI system using a spectrograph that captures the entire field of view in which each pixel of the image contains hyperspectral data from 400-1000nm. Samples were placed on a glass slide and imaged with a 100x oil immersion objective. A reference spectral library for LCO was created by collecting spectral data from a suspension of LCO and then searching algal samples that had been exposed to 1 $\mu g \cdot mL^{-1}$ LCO. The spectral analysis was done using the ENVI software to identify the presence of LCO particles associated with the algal cells, and the Spectral Angel Mapping algorithm was used to show the presence of the particles.

Statistical Analysis.

Statistical analyses were performed using R Studio.[30,31] A Shapiro-Wilk test was performed to determine whether the respective data sets were normally distributed, and a One-Way ANOVA with a Tukey post-hoc test was used to compare the means of normally distributed data. A non-parametric Kruskal-Wallis test with a Dunn's post-hoc test was used to compare the means of non-normally distributed data. In each case, a 95% confidence interval was used to determine significant differences within a data set. Additionally, to compare growth inhibition results to biovolume results, a Pearson coefficient was constructed using R Studio.

1.4. Results and Discussion

LCO Characterization.

LCO is a type of complex metal oxide nanomaterial with a sheet-like morphology comprised of intercalating layers of lithium and cobalt oxide. TEM sizing of single LCO particles suggests an average thickness and length of 5.54 ± 2.01 nm and 39.63 ± 17.35 nm, respectively (**Figure 1**).

The zeta-potential values for LCO suspended in algal complete media indicate that this nanomaterial is highly negatively charged at higher concentrations like 1 $\mu g \cdot mL^{-1}$ (−22.73 mV) and 10 $\mu g \cdot mL^{-1}$ (−30.33 mV), while becoming much less negatively charged at lower concentrations like 0.1 $\mu g \cdot mL^{-1}$ (-10.07 mV) and 0.01 $\mu g \cdot mL^{-1}$ (-2.01 mV). These results suggest that there's an increasing degree of repulsion between LCO nanoparticles with increasing concentrations,[32] and since electrostatic repulsion is one of the primary sources of nanomaterial stability in aqueous media, this would indicate that LCO, in theory, is increasingly stable at higher concentrations when suspended in the complete media and therefore less prone to forming aggregates at those concentrations.[33] However, in practicality, this isn't necessarily the case as visible aggregates can be seen in treatments as low as 1 $\mu g \cdot mL^{-1}$ post exposure, which indicates a lack of stability. Furthermore, it's worth noting that in other types of exposure media like MHRW, LCO also tends to aggregate and settle as well, thus lacking stability in suspension.[10]

Growth Inhibition and Biovolume.

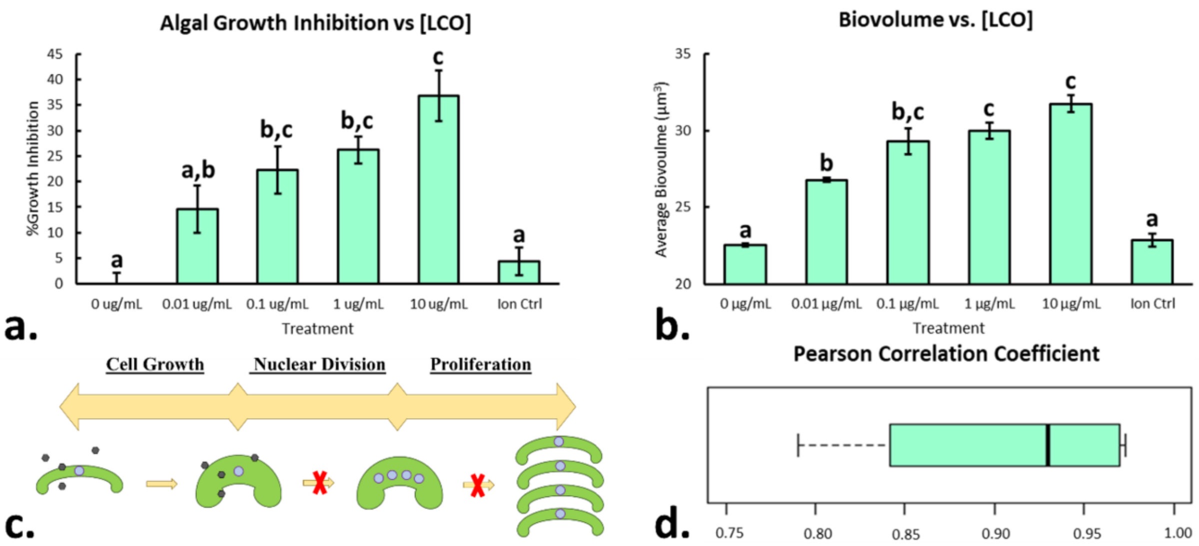

Figure 4: Algal growth and biovolume. (a.) Algal growth inhibition and (b.) average biovolume in response to varying concentrations of LCO after 48 hours of exposure. Significant differences were determined using a one-way ANOVA with a Tukey post-hoc for multiple comparisons; columns with different letters differ significantly ($p<0.05$). Error bars represent SEM. (c.) Simplified diagram of interrupted *R. subcapitata* cell cycle when exposed to LCO. (d.) Pearson coefficient correlation between algal growth inhibition and average biovolume across four replicates.

The level of growth inhibition experienced by LCO-treated cells increased in a dose dependent manner, with significantly higher levels of growth inhibition in comparison to the control at concentrations as low as 0.1 $\mu g \cdot mL^{-1}$ (**Figure 4a**). This is a first-line indicator that LCO induces a toxicological stress response on these algal cells that either causes a decrease in cellular proliferation or an increase in cell death. Furthermore, based on the growth inhibition data, the EC_{50} was calculated to be around 0.057 $\mu g \cdot mL^{-1}$. In the control, cells had an average biovolume of about 22 μm^3, which is consistent with what's reported in the literature for normal biovolumes of this cell type.[26] However, the average biovolume seems to also increase in a dose dependent manner with significant increases to cell size at concentrations as low as 0.01 $\mu g \cdot mL^{-1}$ (**Figure 4b**). These larger biovolumes, while only a direct measurement of cell morphology, may indicate a more serious issue in terms of cell health. *R. subcapitata* cells go through several stages of their cell cycle in which they increase in size, replicate their nuclei, and release multiple, smaller, daughter cells (**Figure 4c**). An increase in the average biovolume may indicate cell cycle interruption/arrest.[24] This is because, for this type of algae, cells that have lost the ability to proliferate, or divide into multiple daughter cells, may still be able to increase in size and/or replicate their nuclei (depending on the cell cycle stage of arrest) as if they were going to proliferate, thus leading to an overall increased average biovolume observed in said populations. When comparing growth inhibition to biovolume, there's an extremely high Pearson correlation between the level of growth inhibition experienced and the average size of algal cells, thus perpetuating the idea that LCO may impact cell cycle progression (**Figure 4d**). This makes sense as inhibitory effects on growth and cell cycle progression would go hand-in-hand. Increased levels of growth inhibition could potentially also be attributed to an increase in senescence, however, assays that directly measure cell death would be needed to validate this prospect. Interestingly, no significant differences in growth inhibition nor biovolume were observed in ion treated cells, this suggesting that LCO induced phytotoxicity is initiated through nano-specific mechanisms, rather than ion-specific mechanisms like in the bacterium, *Shewanella oneidensis*.[34]

Net Carbon Biomass Production.

Unlike growth inhibition and biovolume, the net production of carbon biomass per cell did not change with respect to concentration in a dose-dependent manner (**Figure 5**). Control cells obtained a net average production of 0.078 pg $C\cdot Cell^{-1}\cdot \mu m^{-3}$ after 2 days while LCO-treated cells, in comparison, had only produced roughly 50% less across the board with significant reductions at concentrations as low as 0.1 $\mu g\cdot mL^{-1}$. These results suggest that even at lower, sublethal, concentrations, LCO induces massive reductions to the net production of carbon biomass in these cells. These reductions may result from an increased inactivation of photosynthetic machinery, thus leading to an overall decrease in CO_2 assimilation;[35] they may also result from an increase in glycolytic activity which has been reported in several other organisms in response to LCO exposure. [11,12,13] Even more likely, however, may be a combination of both as an imbalance between carbohydrate production and carbohydrate consumption. Either way, since entire food webs are dependent on primary producing organisms to drive nutrient cycles and energy flow in freshwater ecosystems,[16] this is concerning as widespread contamination of LCO could possibly mean largescale restructuring of ecosystem dynamics and energy budgets.

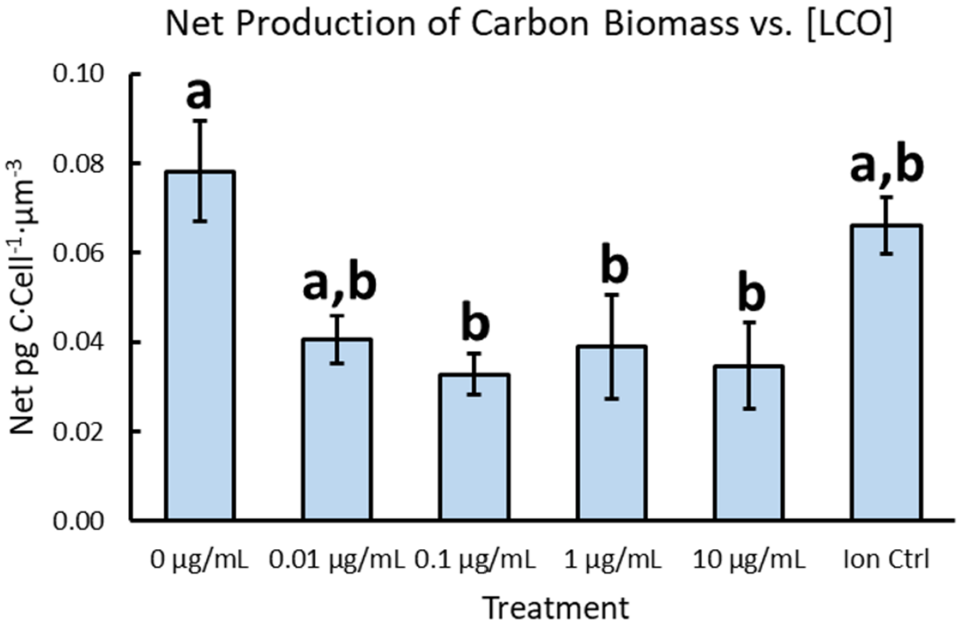

Figure 5: Net production of carbon biomass in response to varying concentrations of LCO after 48 hours of exposure. Significant differences were determined using a one-way ANOVA with a Tukey post-hoc for multiple comparisons; columns with different letters differ significantly ($p<0.05$). Error bars represent SEM.

Neutral Lipid Content.

Microalgae are known for their ability to produce large quantities of neutral lipids called Triacylglycerol, or TAG, and its biosynthesis is largely thought to serve as an energy storage, much like starch.[36] Under optimal conditions, microalgae don't actually produce very much TAG as it's a less preferred form of carbon storage compared to starch, but when they're subject to certain stressors and nutrient deprivation, it causes them to significantly increase their TAG content. Most notably, *Chlamydomonas reinhardtii* has been shown to significantly increase TAG production in response to nitrogen starvation.[37] When exposed to these stressors, there ends up being a shift in their metabolism that favors the production and accumulation of TAG over starch, however, the reasoning behind this is not quite clear.[38] Although, since fatty acids have a higher energy/mass ratio with a higher energy return upon fatty acid oxidation (almost 6.7 ATP equivalents per C) compared to glucose oxidation (about 5.3 ATP equivalents per C), TAG accumulation may be more beneficial in times of energy starvation/ATP deficiencies.[36] TAG accumulation is also especially present in quiescent cells, which are cells that aren't actively dividing, but their photochemistry is still active to some extent.[39]

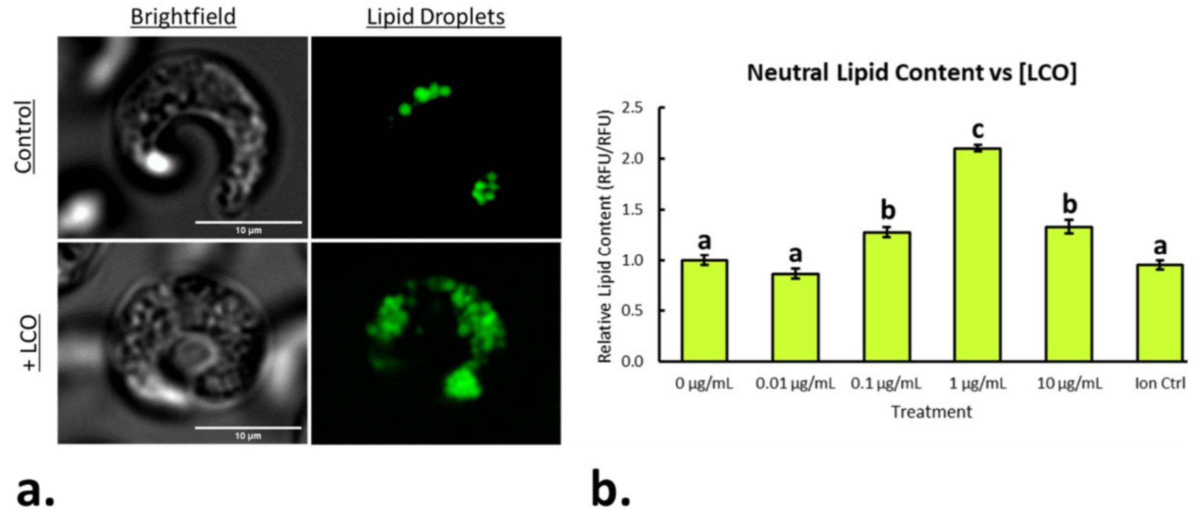

Figure 6: Neutral lipid content. (a.) Representative fluorescence micrograph of a control cell (top) and an LCO treated cell (bottom, 1 $\mu g \cdot mL^{-1}$). (b.) Relative neutral lipid content in response to varying concentrations of LCO after 48 hours of exposure. Significant differences were determined using a one-way ANOVA with a Tukey post-hoc for multiple comparisons; columns with different letters differ significantly ($p<0.05$). Error bars represent SEM.

As displayed in **Figure 6a**, a representative fluorescence micrograph depicts a control cell (top), containing a minimal amount TAG content, in comparison to an LCO-treated cell (bottom, 1 $\mu g \cdot mL^{-1}$) which has produced a seemingly larger amount of TAG. Further validating this observation, the microplate assay results in **Figure 6b** roughly exhibit a positive correlation between LCO concentration and relative neutral lipid content. A significant peak production is seen at 1 $\mu g \cdot mL^{-1}$ of LCO with over a 100% increase in TAG content compared to the control. However, once again, no significant increase in TAG production was observed in ion treated cells. These results suggest that LCO exposure leads to a metabolic shift in these cells which favors the production and accumulation of TAG over starch, and thus may be indicative of an interference to their energy and central carbon metabolism.[28] One factor leading to this increase in TAG production may be due to the presence of Co^{2+} in LCO. Other algal species like *Chlorella vulgaris*, for example, have been reported to increase their production of TAG when exposed to heavy metals like cobalt.[38] Although, in this case, this would only be true for Co^{2+} in the nano form, as opposed to the ionic from.

Single-Cell Chlorophyll Fluorescence Microscopy.

High-content fluorescence imaging was first used to visually inspect LCO-induced changes to cell morphology. The morphology of LCO-treated cells (**Figure 7c-d**) appear larger in size compared to the control cell (**Figure 7a**), aligning with results in **Figure 4b**. LCO-treated cells also appear to have more of a “French croissant”-type shape (**Figure 7d**), similar to that of algae cells exposed to metolachlor, as described by Machado & Soares, 2020. Other 2D nanomaterials, like graphene-oxide, have previously been reported to elicit mechanical disturbances to the cell by damaging the membrane with their sharp edges.[40] However, when comparing the morphology of LCO-treated cells to that of the Carfentrazone-treated cell (**Figure 7b**), used as a positive control

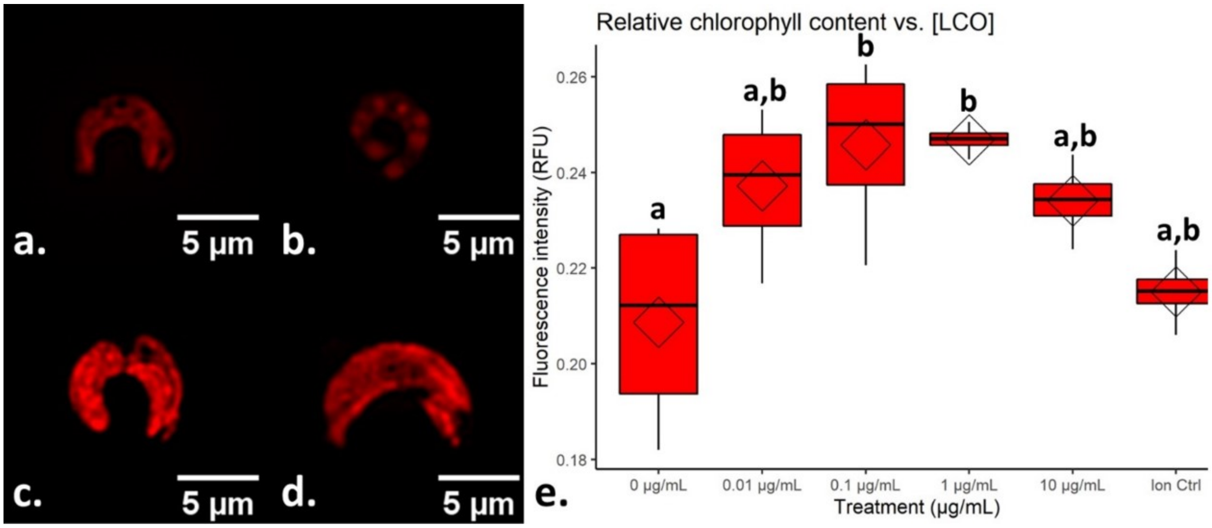

Figure 7: Single-cell chlorophyll fluorescence. Representative fluorescence micrograph of (a.) a control cell, (b.) a Carfentrazone-treated cell used as a positive control for membrane damage, and a lithiated cobalt oxide (LCO)–treated cell exposed to (c.)1 μgml^{-1} LCO and (d.)10 μgml^{-1} LCO. (e.) Relative chlorophyll content in response to varying concentrations of LCO after 48 h. Bars on boxplots represent treatment medians, while diamonds represent treatment averages. Significant differences were determined using a one-way analysis of variance with a Tukey post hoc test for multiple comparisons; columns with different letters differ significantly ($p < 0.05$). RFU = relative fluorescence unit.

for membrane damage,[41] their morphologies appear quite different. While the LCO-treated cells look larger and brighter compared to the control, they still appear to uphold the structural integrity of their membrane. By contrast, the morphology of the membrane damaged positive control appears to have lost its structural integrity while displaying more of a “stringed pearls”-type shape. Furthermore, high-content fluorescence imaging and bioimage analysis were also employed to quantify the emitted fluorescence intensities of individual cells, which are proportional to the abundance of chlorophyll within those cells. LCO-treated cells appear to have higher fluorescence intensities, and thus increased chlorophyll content, relative to the control, with significant increases at 0.1 & 1 $\mu g \cdot mL^{-1}$ LCO (**Figure 7e**). This is contrary to other types of metal oxide nanomaterials which have been reported to decrease chlorophyll content.[42] However, in the event of photosynthetic inhibition, cells are likely to produce more chlorophyll to maximize light harvesting.[43]

Enhanced Dark-Field Hyperspectral Imaging

Enhanced dark-field microscopy coupled with hyperspectral imaging was employed to visualize the interactions of LCO particles with the algal cells. LCO deposits, visible as white pockets of scattered light, can be seen internalized within the LCO-treated cells (**Figure 8f**). These LCO deposits are only visible on the same Z-focal plane as the cells (i.e., not above or below) and are not seen on their outer perimeter, thus suggesting that LCO actually enters the cells rather than just adhering to the outer surface. No LCO deposits were identified within the control cells (**Figure 8c**). A spectral reference library for LCO was constructed using a samples of LCO particles in algae media and samples of LCO-treated algae (**Figure 8a**). The spectral angle mapping algorithm identified pixels, mapped in red, that matched the LCO spectra, thus verifying the presence of LCO deposits in the LCO-treated algal cells (**Figure 8g**). As expected, these spectra were not identified in the control cells, and therefore no mappings were generated (**Figure 8d**). The mechanism of internalization is unclear, however the vesicular shape of the tightly packed LCO deposits (**Figure 8f**) may suggest uptake through endocytosis. Yan et al., 2021 reported that the uptake of AIE functionalized Ag nanoparticles, with a similar zeta-potential and aggregational behavior to LCO, were mediated through clathrin-dependent endocytosis.

Each of the parameters tested in this chapter are metabolically related to one another and can influence larger ecosystem outcomes. For example, the amount of net carbon biomass produced by individual cells will determine how much energy is available to sustain their routine cell maintenance. And should the cells become energy deficient, they may not be able to sustain energy intensive processes like cell division, thus causing them to enter a state of quiescence. Cells in this

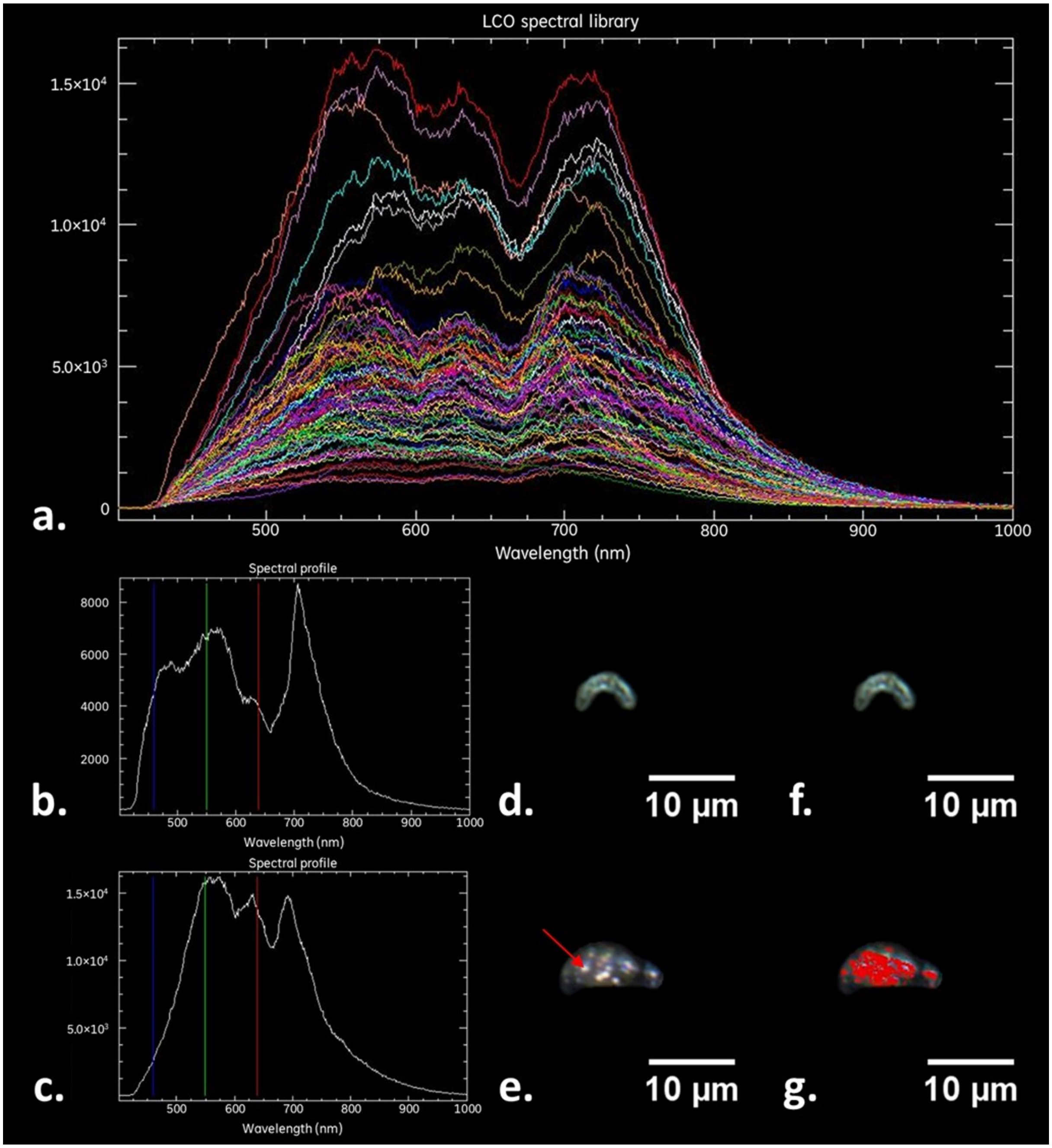

<u>Figure 8</u>: Enhanced dark-field hyperspectral imaging of LCO-treated cells. (a.) Reference lithiated cobalt oxide (LCO) spectra library. Spectra generated by (b.) a control cell and (c.) an internalized LCO deposit from a cell exposed to 1 μgml^{-1} LCO. Representative darkfield micrograph of (d.) a control cell and (e.) a cell exposed to 1 μgml^{-1} LCO; the red arrow points to an internalized LCO deposit. Representation of the spectral angle mapping algorithm used to identify pixels matching the LCO spectral library in (f.) a control cell and (g.) a cell exposed to 1 μgml^{-1} LCO; pixels matching the LCO spectral library are mapped in red.

sort of state could foster larger biovolumes as they would've lost the ability to proliferate, and to accumulate neutral lipids like TAG due to a shift in their central carbon metabolism. Ultimately, this would also lead to a decline in phytoplankton communities. And then over time, with a reduction in the amount of carbon biomass being produced per cell, and with diminished phytoplankton availability in general, this could significantly alter ecosystem energy budgets.

In this chapter, as hypothesized, facets of algal physiology related to growth and energy production were negatively impacted in response to LCO. Negative impacts to growth were exhibited by a significant increase in growth inhibition and biovolume, which indicates an increase in cell cycle disturbances. Negative impacts to energy production were exhibited by a significant decrease in the net production of carbon biomass, as well as a significant overproduction of TAG, which indicates interference with CO_2 assimilation chemistry and/or carbon partitioning. Relative chlorophyll content, however, was significantly increased. While increased chlorophyll content could be considered an enhancement to photosynthesis, as argued by Zhang et al., 2021, this may be more indicative of a compensatory action to increase light harvesting in this case as the amount of carbon biomass was still negatively impacted. Interestingly, though, cells that were treated with dissolved Li^+/Co^{2+} ion controls were not significantly impact in any of the endpoints tested, which suggests that LCO phytotoxicity is mediated through nano-specific mechanisms rather than ion-specific. The reason for this is unclear, especially since engineered nanoparticles tend to behave unpredictably in complex biological media. However, with its unique physiochemical properties and high surface area-to-volume ratio, it's possible that LCO could obtain certain surface modifications/protein coronas in its nano form that make it interact more favorably with cells in comparison to its ionic form.[46]

These responses clearly demonstrate the adverse impacts of LCO on the physiology of *R. subcapitata* and suggest a likely disruption of key metabolic processes relating to cell growth and energy production/metabolism. One possible mechanism that may initiate the observed toxicological responses is the likely ability of LCO to participate in redox reactions, especially with iron containing proteins, as it was determined in *C. riparius*.[11] This could also be possible for algae as cellular uptake of LCO nanoparticles was observed with enhanced dark-field hyperspectral imaging.

In study by Niemuth et al., 2019 found *Chironomus riparius* exposed to LCO had a significantly decrease in the function of the iron-containing protein, hemoglobin. This was supported both quantitatively from green absorbance and qualitatively from the loss of their deep red color to a pale-yellow color (their natural red color is due to the presence of heme proteins). This is concerning as proteins with heme and iron-sulfur centers are important for the transfer of electrons in many essential life processes like respiration, and in the case of algae, photosynthesis as well.[47]

One such protein with an iron-sulfur center involved in the process of photosynthesis is Ferredoxin. In a study done by Isabel and José Moura, they were able to use electron paramagnetic resonance to prove that in the Ferredoxin II protein from *Desulfovibrio gigas*, cobalt was able to be incorporated into the vacant site of the iron-sulfur cluster, thus reducing it to a $CoFe_3S_4$ cluster.[48] It's possible that similar phenomena could be happening with the cobalt from the LCO, in which case causing a conformational change in those iron-sulfur proteins that change their overall chemistry. This could be especially harmful to the function of the iron-sulfur proteins involved in respiration and photosynthesis as they must remain in an oxidized state to be able to accept and transfer electrons in their respective electron transport chains, which is needed to produce ATP, as well as NADPH in photosynthesis. Since life is dependent on the movement of electrons, a short in this biochemical circuit could reduce the efficiency of the cell's ability to conduct life processes like photosynthesis, which would help explain the decreased net production of carbon biomass, as well as the increase in growth inhibition for LCO-treated cells.

Heavy metal contaminants, in general, have been seen to inhibit primary productivity in aquatic environments.[49] However, cobalt itself has been reported to decrease the growth of green algae at concentrations as low as 0.6 $\mu g \cdot mL^{-1}$.[50,51,52] Additionally, cobalt has also been reported to decrease the amount of O_2 evolution in green algae at certain concentrations, and has been seen to directly target PSII, meaning that cobalt can and does interfere with electron transport and photosynthetic efficiency.[51,52] This further supports the idea that the cobalt from LCO could be an initiator for adverse outcomes observed in eukaryotic organisms that have been exposed to this type of nanomaterial.[10]

Other 2D-nanomaterials like graphene-oxide, have been reported to have different, physical, mechanisms of toxicity relating to membrane damage, nutrient depletion, and by covering the surface of, and therefore shading, the cell.[40] In terms of membrane damage and cell surface covering, these occurrences were proven to not be the case for LCO through microscopic observation. Fluorescence imaging showed a discrepancy between the morphology of LCO-treated cells and membrane damaged positive control cells, thus suggesting that LCO does not cause membrane damage. Additionally, enhanced dark-field hyperspectral imaging revealed that while cells were internalizing LCO nanoparticles, they were not simply adhering to/covering the surface of the cell. This makes sense as the surface charge of LCO and cell membranes are electrostatically incompatible. For example, Kim et al., 2022 reported with QCM-D that negativley charged nanodots do not interact/adhere to negatively charged plant bio-surfaces due to electrostatic incompatibilities. But in terms of nutrient depletion, LCO has been reported to adsorb nutrients like phosphate,[20] which could, in theory, partially explain some of the disturbances. However, in cases of nutrient depletion, algae also typically undergo chlorosis as they are related to one another.[54] Not only was this not the case for LCO-treated cells, but the opposite trend was actually observed, thus suggesting that nutrient depletion is not a major factor for LCO-induced toxicity in algae.

Overall, this chapter demonstrates that LCO significantly alters different aspects of *R. subcapitata* physiology even at lower, sub lethal, concentrations, and therefore may also likely pose a risk to other types of phytoplankton as well. Most concerning is LCO's impact to algal growth and net primary productivity, which could have several ecologically related implications. Primarily, altering the efficiency of phytoplankton productivity could impact the sustainability of freshwater ecosystems. Thus, widespread contamination of LCO to freshwater ecosystems would likely limit the amount of nutrients and chemical energy needed to support all life in those systems by decreasing the density of phytoplankton communities and their associated productivity at the cellular level.

1.5. Acknowledgement

This material is based on the work supported by the National Science Foundation, Center for Sustainable Nanotechnology (CSN; grant CHE-2001611). The CSN is part of the Centers for Chemical Innovation Program.

Chapter 2.

Using a novel multiplexed algal cytological imaging (MACI) assay and machine learning to characterize complex phenotypes in plant-type organisms.

2.1. Abstract

High-throughput phenotypic profiling assays, popular for their ability to characterize alternations in single-cell morphological feature data, have been useful in recent years at predicting cellular targets and mechanisms of action (MoAs) for different chemicals and novel drugs. However, this approach has not been extensively used in environmental toxicology due to the lack of studies and established methods for performing this kind of assay in environmentally relevant species. In this chapter, methods were developed for a multiplexed cytological imaging (MACI) assay, based on the subcellular structures that are unique to microalgae, like *Raphidocelis subcapitata*. Several different herbicides and antibiotics with unique MoAs were exposed to *R. subcapitata* cells and MACI was used to characterize cellular impacts by measuring subtle changes in their morphological features, including metrics of area, shape, quantity, fluorescence intensity, and granularity of individual subcellular components. This study demonstrates that MACI offers a quick and effective framework for characterizing complex phenotypic responses to environmental chemicals that can be used for determining their MoAs and identifying their cellular targets in plant-type organisms.

2.2. Introduction

With increasing quantities and classes of contaminants, including engineered nanomaterials, introduced into commerce and therefore found in the environment, there is a call for more rapid techniques for evaluating their potential hazards in a quick and efficient manner. Specifically, there is a need for more nontargeted, high-throughput profiling assays that can characterize biological activity, identify potency thresholds, and predict mechanisms of action (MoAs).[55] In recent years, morphological/phenotypic profiling has been shown to provide rich sources of data for interrogating biochemical perturbations as the morphology of a cell is extremely sensitive and strongly influenced by factors such as metabolism, genetic state, and environmental cues.[56] Additionally, it has been shown that specific biological perturbations deliver specific phenotypic profiles, and therefore any subset of morphological features that deviate from that of healthy cells can serve as a fingerprint to characterize biological activity.[57] Furthermore, when comparing the fingerprint of cells treated with novel compounds to that of cells treated with compounds with previously established MoAs, the probable MoA of these novel compounds can then be identified.[58]

Common high-throughput phenotypic profiling assays, like the Cell Painting Assay[59], involve the use of multiplexed fluorescence cytochemistry to visualize multiple subcellular structures within a cell and high-content imaging to take hundreds of snapshots of their morphology in an automated and consistent manner. These image data can then be converted into quantitative data by using bioimage analysis to extract hundreds of morphological features at the resolution of a single cell. These morphological features include metrics related to cell size, shape, fluorescence intensity, texture, granularity, and even spatial relationships between organelles which all represent subtle unbiased descriptors of the phenotypic state. Currently, high-throughput phenotypic profiling assays are used most often in the context of drug discovery and disease models. For example, Hughes et al. (2020) used Cell Painting to screen 19,555 compounds and profile the phenotypic response across several esophageal adenocarcinoma cell lines. In doing so, this study successfully identified novel drug targets, MoAs, and pharmacological classes that targeted that specific type of cancer. However, this kind of assay may also have applications in other fields like eco- and environmental toxicology.

Recently, the Unites States Environmental Protection Agency (USEPA) has begun to use high-throughput phenotypic profiling for the screening and hazard identification of environmental chemicals, however, only human-derived cell models are still largely being used for this purpose.[57,61] While human-derived cell models provide the advantage of proven characterization and predictive power, they may not accurately represent phenotypic responses in environmentally relevant species, like plants and algae, whose cells are biologically distinct from animal cells. For example, DCMU (3-(3,4-dichlorophenyl)-1,1-dimethylurea), or Diuron, has been reported to cause DNA damage in certain types of human cancer cell lines[62] but in plants and algae targets photosystem II (PSII) proteins.[63] Furthermore, human cell lines may not accurately represent environmentally safe exposure levels for certain compounds, like ZnO nanoparticles, that are relatively benign to humans,[64] but acutely toxic to algal species at low concentrations.[65] Thus, cell models which are more environmentally relevant should be considered. In particular, *Raphidocelis subcapitata*, a prevalent type of freshwater green algae and an environmentally relevant organism, is a good candidate model to use for high-throughput phenotypic profiling as it is a USEPA established model for environmental toxicology[14] and an important bioindicator species for assessing/monitoring water quality.[66] Additionally, its strictly unicellular nature makes it beneficial for image-based assays in terms of downstream bioimage segmentation, which may be more difficult to do for other common microalgae like *Chlamydomonas spp*., *Chlorella* spp., and *Scenedesmus spp*. that tend to form colonies or coenobia under stress.[67,68]

Here we describe a multiplexed algal cytological imaging (MACI) assay for the phenotypic profiling of environmental chemicals, based on three subcellular structures that are important for the architecture of *R. subcapitata* cells: the chloroplast, nuclei, and lipid droplets. Each of these subcellular structures represent a different aspect of algal physiology and can be used to characterize complex phenotypes and predict phytotoxic mechanisms of action. For example, the chloroplast is an important subcellular compartment for conducting photosynthesis, and features related to chloroplast fluorescence can be used to describe relative levels of chlorophyll content between treatments, and can even be used to calculate the quantum yield of PSII.[69] Nuclei play a crucial role in regulating gene expression and facilitating cellular division, and features related to the number on nuclei per cell, as well as the relative amount of DNA content per nucleus, can be used to describe instances of cell cycle disruption/arrest.[67,70] And lastly, lipid droplets, which are a collection of neutral lipids, often triacylglycerol (TAG), and serve as an alternative form of energy storage to starch, are often indicators of cell stress when accumulated in large quantities.[39]

As a proof of concept, this study aims to assess the ability of the MACI assay to characterize and differentiate between cells which were exposed to various compounds with unique MoAs. The performance of this assay was evaluated by testing a small reference set of herbicides and antibiotics, which have been previously annotated, and preforming a hierarchical clustering analysis of their phenotypic fingerprints. Additionally, a convolutional neural network (CNN) machine learning model was trained off of a small subset of cell image data in order to predict compound-specific perturbances. We propose that the MACI assay is a quick and effective way to characterize complex phenotypes and predict interactions with environmentally relevant chemicals in plant-type species.

2.3. Materials and Methods

Algal Cell Culture.

A stock culture of *R. subcapitata*, inoculated at 1×10^5 Cells·mL^{-1}, was grown in a 1 L Erlenmeyer flask and cultured in OECD 201 media [21]. Cells were illuminated continuously with a full spectrum T8 light bulb at a photon flux of 70 μE·m^{-2}·s^{-1}. The stock culture was mixed with an orbital shaker at a speed of 111 rpm.

Exposure Setup.

Eight different reference chemicals with unique established MoAs (described in **Table 1)**, were exposed to cells for 24 hours at either 0 (control), 0.1, 1, or 10 μM.

Table 1: Reference Chemicals with Known MoAs

Chemical	Mechanism of Action	Abbreviation	References
Aclonifen	Carotenoid Biosynthesis Inhibition	CBI	71
Carfentrazone	Membrane Disruption	MD	41
DCMU	PSII Photochemistry Inhibition	PPI	72
Glufosinate	N_2 Metabolism Inhibition	NMI	73
H_2O_2	Oxidative Stress	OS	74
Metolachlor	Very-Long-Chain Fatty Acid Synthesis Inhibition	VLCFASI	24
MSMA	OP Uncoupler/e$^-$ Transport Inhibition	OPU/e$^-$TI	75
Zeocin	DNA Damage	DD	76

Each chemical was solubilized in either OECD 201 medium or 100% EtOH depending on its polarity, and sonicated for 30 minutes to prepare a primary 1000 μM stock. A secondary 100 μM stock solution was then prepared for each chemical by preforming a serial dilution from their respective primary stock solution into OECD 201 media. While cells were growing exponentially, 900 μL aliquots of algal stock culture were seeded into individual 1.5 mL microcentrifuge tubes.

For each treatment, done in quintuplicate, the respective secondary stock solution and/or OECD 201 medium was added to each 900 µL cell suspension at a final volume of 1 mL. Resulting EtOH content in final exposure samples (≤ 1%) had a negligible effect on cell morphology (**Supplementary Figure S4**). The samples were then placed under full spectrum illumination, with tube lids open, at a photon flux of 70 $\mu E \cdot m^{-2} \cdot s^{-1}$ for 24 hours. 24 hours was chosen for the exposure duration as this timepoint has been shown to better delineate initial phenotypic impacts,[61] however, longer timepoints can also be chosen depending on the purpose of the exposure.

Multiplexed Algal Cytological Imaging (MACI) Assay.

At the conclusion of the exposure, 905 µL aliquots from each sample were transferred to sterile 1.5 mL microcentrifuge tubes. Commercially available fluorescent probes and glutaraldehyde were used to stain and fix multiple subcellular compartments of the algal cells. The chloroplast is auto fluorescent due to the presence of chlorophyll, and thus did not require a fluorescent probe, but NucBlue (Thermo Fisher, R37605) was used to label nuclei and BODIPY 505/515 (Thermo Fisher, D3921) was used to stain neutral lipid droplets, as seen in **Figure 9**. Reagent quantities, listed in **Table 2**, were added to each cell suspension at a final reaction volume of 1 mL.

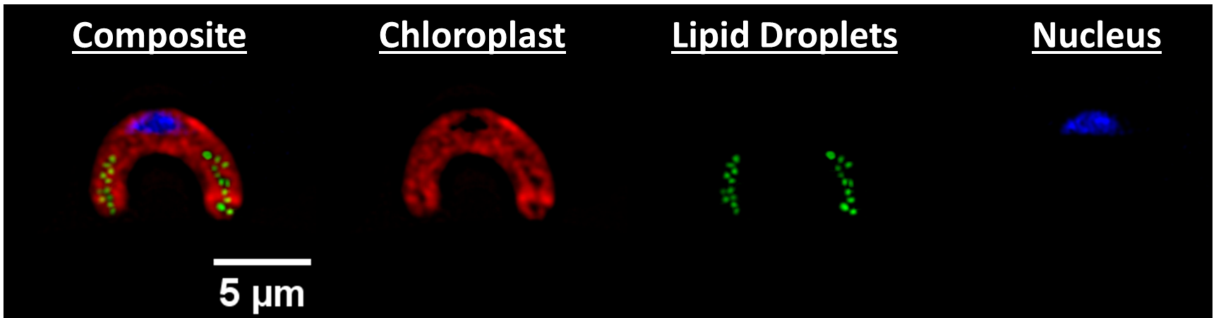

Figure 9: The MACI assay as seen in a *Raphidocelis subcapitata* cell. Representative fluorescence micrograph where each column represents a different fluorescently labeled subcellular compartment visualized by the MACI assay.

Table 2: Reagent Quantities for 1 mL Reactions

Reaction Component	**Quantity**	**Final Concentration**
Cell Suspension	905 μL	N/A
NucBlue	2 Drops (~84 μL)	N/A
BODIPY 505/515	1 μL	5 μM
Glutaraldehyde	10 μL	0.025% - 0.25%
Total	**1 mL**	**N/A**

After adding reagents, all reactions should be incubated for at least 1 hour, or overnight, at 4 °C to minimize enzymatic degradation and maintain the integrity of the subcellular structures. Cells can also be stored at 4 °C for as long as one week when fixed with higher concentrations of glutaraldehyde (~0.25%) for maximum recovery (Shapiro et al., 2001). Alternatively, for live cell imaging, all reagents, excluding glutaraldehyde, should be added, and reactions should be incubated in the dark at room temperature for 15-30 minutes. After incubating reactions, cells were centrifuged at 4000 x g for 5 min, washed 2x with 1X Phosphate Buffered Saline (PBS), and resuspended in PBS. Cells from each sample were loaded into a well of a glass bottom 384 well plate (Cellvis, P384W-1.5H-N) at a seeding density of ~2 $\times 10^3$ cells$\cdot$mm^{-2} for optimal distribution of cells across the well surface. After loading cells, the well plate was then spun gently at 600RPM for 1 minute to concentrate cells at the bottom of the well. Alternatively, loaded well plates can also be set aside for 30-60 minutes at room temperature to allow cells to settle before imaging. Images were acquired at 9 sites per well with an ImageXpress Micro XLS High-Content Screening System with a 60X Plan Fluor 0.85 NA air immersion objective (Molecular Devices, 1-6300-0414), using the fluorescent channels described in **Table 3**.

Table 3: MACI Fluorescence Cytochemistry parameters

Organelle	Stain	Channel	Excitation (nm)	Emission (nm)
Chloroplast	Auto Fluorescent	Cy5	628/40	692/40
Lipid Droplets	BODIPY 505/515	GFP	472/30	520/35
Nuclei	NucBlue	DAPI	377/50	447/60

To enhance image contrast and resolution, the digital confocal feature was used during image acquisition. For representative cell images with higher resolution, some images were also acquired with a 100X CFI L PLAN EPI CC 0.85 NA air immersion objective (Molecular Devices, 1-6300-0419).

Bioimage Analysis.

After acquiring images, any image analysis software can be used to extract quantitative data from the images. In this study, CellProfiler,[29] an open-source modular bioimage analysis software, was used for image pre-processing, object segmentation, and morphological feature extraction at the resolution of individual cells. The pipeline identifies the chloroplast from the Cy5 channel, which spans most of the cell area of *R. subcapitata*, to help aid a segmentation algorithm in identifying individual cells, or regions of interest (ROI). These ROI are then used as a mask to identify which subcellular structures belong to which cell. This pipeline extracts 450 unique morphological features per cell related to area, shape, intensity, and granularity of each subcellular structure, which is then exported to a local SQLite database file. Data tables were extracted from the SQLite database file using the RSQLite package in R.[78]

Phenotypic Profiling - Fingerprint Analysis.

Phenotypic response data was analyzed using a general phenotypic profiling workflow (**Figure 10**). Data was firstly processed by aggregating single-cell morphological feature measurements to per-image and then per-well values, which was done by taking the cell and image means, respectively. Secondly, well data from each compound and dose were then normalized to the non-treated cell control by computing a Z-score:

$$Z - score = \frac{x-\mu_{ctrl}}{\sigma_{ctrl}}\ldots\ldots\ldots\ldots\ldots\ldots(5)$$

where x is the feature value, μ_{ctrl} is the mean feature value of the control, and σ_{ctrl} is the standard deviation of the feature value of the control. In order to verify whether each reference compound elicited a change to the entire phenotypic profile of treated cells and to characterize compound-specific phenotypic changes, a partial least squares-discriminant analysis (PLS-DA) was

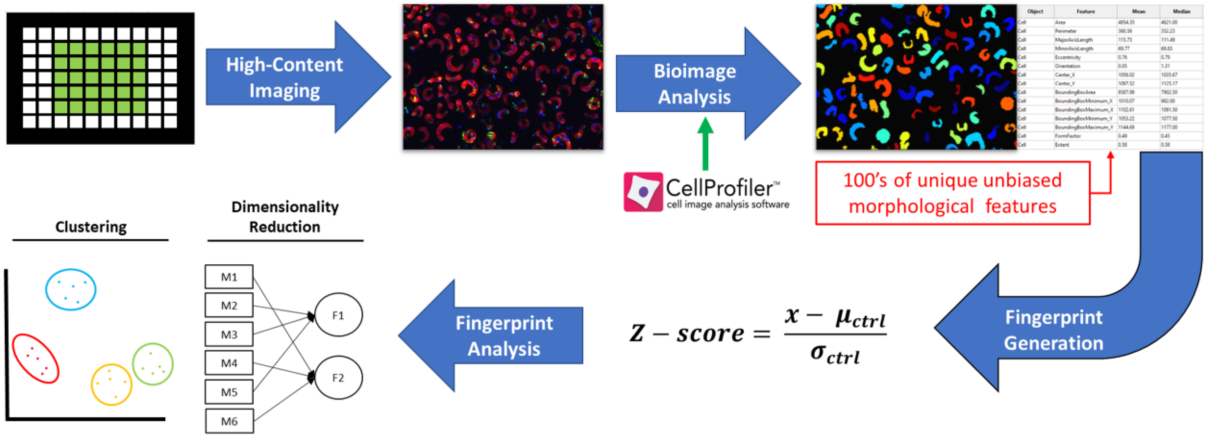

Figure 10: Phenotypic profiling workflow. General overview of the steps taken to conduct phenotypic profiling using image-based data. After perturbing and staining the algae cells, they are seeded into a 384-glass bottom well plate for high-content imaging. A CellProfiler pipeline (or a pipeline from any image analysis software) is used to convert the image data into quantitative data at the resolution of a single cell. Phenotypic fingerprints are then generated by calculating z-scores, and analyzed by reducing data dimensionality and/or preforming a clustering analysis.

performed in R using the mixOmics package.[79] Before feeding phenotypic response data into the PLS-DA models, an ANOVA was performed across all features for each refence chemical to remove any non-informative features with little variance (p-values > 0.05). Lastly, factor analysis was used to further reduce the dimensionality of phenotypic data vectors, and the fingerprints were subsequently compared to one another using hierarchical clustering based on Pearson correlation in R.

Phenotypic Profiling - Convolutional Neural Networks.

In addition to fingerprint analysis, a CNN was also trained on a small subset of reference compound treated cells (~10.5%) using the classifier module on CellProfiler Analyst (Ver 3.0).[80] A separate bin was created for each reference chemical and the non-treated cell control in the classifier module, where around 1000 randomly fetched cells from each treatment were placed in each respective bin **(Figure 12)**. After training the CNN, it was used to score the entire experiment by classifying individual cells into predicted mechanistic classes, and computing enrichment scores for each sample as the logit area under the receiver operating characteristic curve. An ANOVA and a Tukey post-hoc test was used to evaluate the significance of predicted mechanistic class enrichments for each treatment.

Statistical Analysis.

All statistical analyses were performed using R Studio [30,31]. A Shapiro-Wilk test was used to verify normal distribution and a One-Way ANOVA was used to compare variance among group means, while a Tukey post-hoc test was used for multiple comparisons. In each analysis, significant differences were determined with a 95% confidence interval.

2.4. Results and Discussion

Different data-analysis strategies can be implemented in the downstream analysis of image-based phenotypic profiling.

Typically, the main goal for interpreting phenotypic profiles is to understand the structure of data relationships, which can be done through the visualization, clustering, and classification of high-dimensional data.[81] Several methods exist for the visualization of high-dimensional data, with principal component analysis (PCA) as one of the most popular methods. PCA is an unsupervised learning and dimensionality reduction analysis that maximizes the variance of projections onto orthogonal components, which can be useful for identifying similarities and patterns in datasets.[79] Another useful method for visualizing high-dimensional data is the partial least squares-discriminant analysis (PLS-DA), which, unlike the PCA, is a supervised learning and dimensionality reduction analysis that maximizes the covariance between predictor variables and class labels.[82] PLS-DA can be useful in the goal of characterizing phenotypic responses with the added advantage of ranking predictor variable importance in projections. Hierarchical clustering is another useful analysis that reveals patterns in the data which is computed through a similarity matrix containing similarity values between each sample.[81] Several popular similarity measurements can be used for clustering, such as cosine similarity or Euclidean distance, however many labs will perform clustering analyses based on Pearson correlation coefficients as they allow for the clustering of pairs, which can be helpful if some compounds elicit the same morphological changes, but to different degrees.[58] These clustering analyses can be useful for separating complex phenotypes and inferring like MoA's through grouping like responses together. Lastly, classification analyses can also be useful for identifying the MoA of novel chemicals by transferring class labels from reference data to unknown data points.[81] Recent advancements have been made in image-based classification with the use of machine-learning algorithms, like convolutional neural networks (CNN). CNNs are powerful as they can predict MoA of unknown chemicals or detect which known chemicals were exposed to cells through a concatenation of layers that are trained to reweight and transform data from raw images.[83]

Complex changes in phenotypes of cells upon chemical exposure can be defined using MACI.

After perturbing cells with respective reference chemicals and conducting MACI, a CellProfiler pipeline was used to convert the high-content image data into quantitative data. From these data 450 unique, unbiased, morphological features were extracted at the resolution of a single cell, which were used to generate phenotypic fingerprints of molecular interaction. In order to verify whether each reference chemical elicited a significant change to cell morphology, we characterized the cellular responses to each reference chemical, individually, by comparing changes in their complex phenotypic profiles with increasing concentration. This was done with a PLS-DA, which is a supervised machine learning algorithm that projects multidimensional datasets onto two-dimensional planes in order to predict responses between groups. Based on the PLS-DA response plots (**Figure 11**), each chemical treatment displays a significant separation between response groups, thereby indicating that each reference chemical does elicit a significant, and measurable, change to cell morphology after 24 hours. Variable importance in projection (VIP) scores were also extracted from each PLS-DA response plot (**Supplementary Table S2**). VIP scores indicate the features, or predictors, which are most influential in driving the separation between response groups and can, therefore, help characterize groups of phenotypic markers that are unique to chemicals with specific MoAs. In this case, predictors with VIP scores above 1.0 were considered most important.

Based on the top 10 VIP scores for each PLS-DA model, response groups of each reference chemical were delineated with a distinct combination of phenotypic markers, thus indicating that MACI can be used to characterize compound-specific interactions. For example, exposure to Aclonifen, a carotenoid biosynthesis inhibitor,[71] was most distinguishable by changes in nuclear shape features while exposure to Metolachlor, a very-long-chain fatty acid synthesis inhibitor,[24] was most distinguishable by changes in features related to lipid droplet granularity. There were also some phenotypic markers that overlapped for certain chemicals. For example, cells treated with H_2O_2 and Zeocin, a DNA damaging agent,[76] both garnered the same top three chloroplast

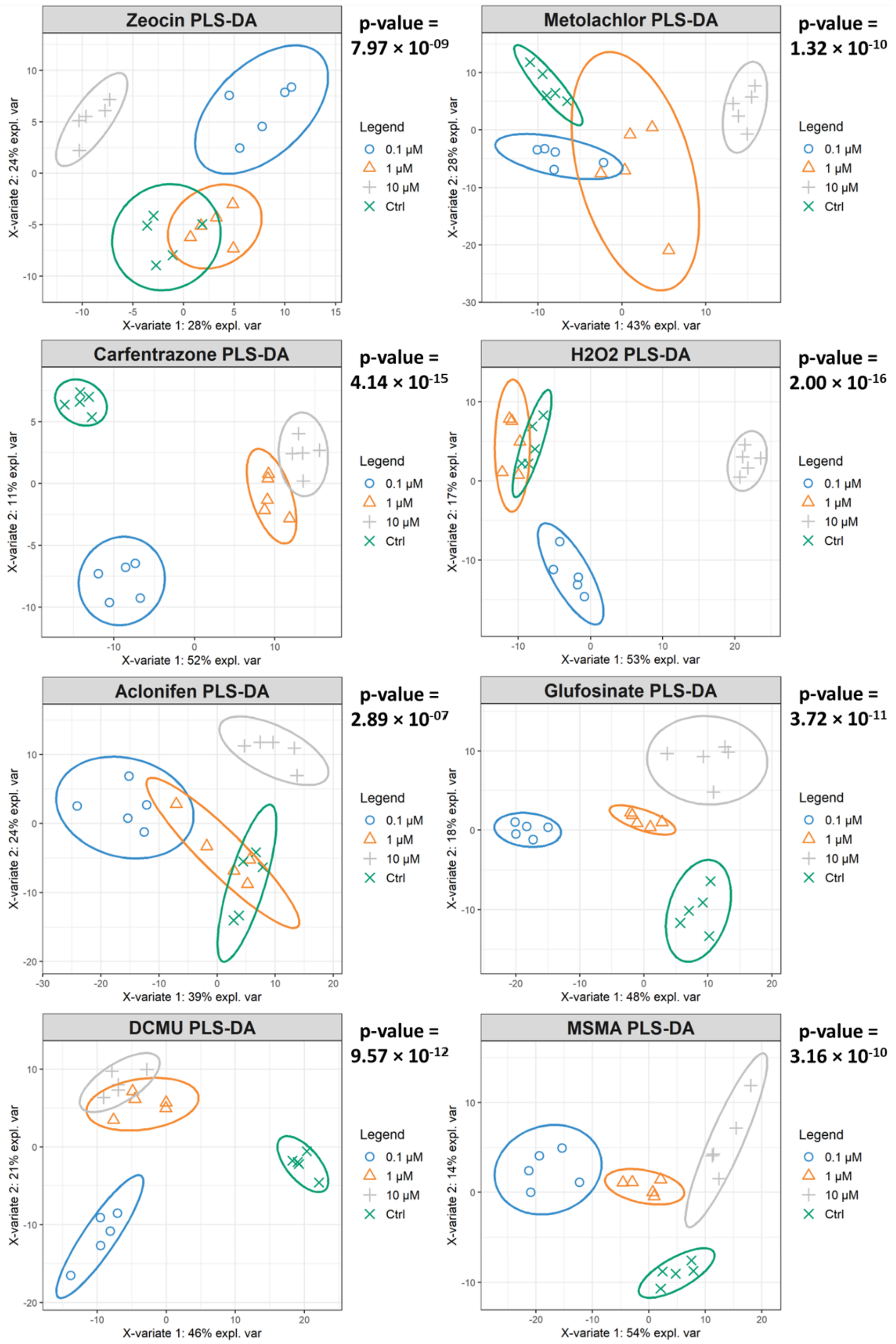

Figure 11: Phenotypic responses to reference chemicals. A partial least squares-discriminant analysis (PLS-DA) response plot for each reference chemical graphically describes the change across complex morphological feature data with increasing concentration; ellipses represent 95% confidence intervals and p-values represent ANOVA statistics across the 1st latent variable between response groups.

normalized moment features. However, the VIP ranking order of these phenotypic markers, as well as the overall combination of markers, were still distinct between chemical profiles. Therefore, when using phenotypic profiling for predicting chemical MoAs, the entire profile, rather than the individual features, should be considered.

Impacts of chemicals can be separated using MACI through hierarchically clustering phenotypic fingerprints.

The ability of MACI to delineate subtle changes in complex phenotypes of chemical-specific perturbance was evaluated, firstly, by comparing the phenotypic fingerprints of each chemical treatment to one another. For this purpose, the 10 μM data was used as this was the concentration that caused the largest change in morphology, compared to the control, for most of the reference chemicals after 24 hours. After constructing the phenotypic fingerprints, an ANOVA was used to identify individual features that carry little information, which were removed from the analysis given a p-value > 0.05. Additionally, factor analysis was used to further reduce the dimensionality of the phenotypic data vectors down to 7 eigen features/factors in order to minimize redundant measurements adding noise while still preserving the variance within the dataset, as suggested by Young et al., 2008. The optimal number of factors was determined with a non-graphical Cattell's scree test.

The phenotypic fingerprints across all replicates for each reference chemical were hierarchically clustered based on their Pearson correlation coefficient in relation to one another (**Figure 12**). The hierarchical clustering analysis was able to identify 8 separate clusters (**Figure 12j.**). All of the clusters grouped individual replicates of the same chemical treatment together, thus indicating high correlation across replicates and reproducibility in cell-chemical interactions. However, some treatments were slightly less robust than others. For example, samples treated with Glufosinate

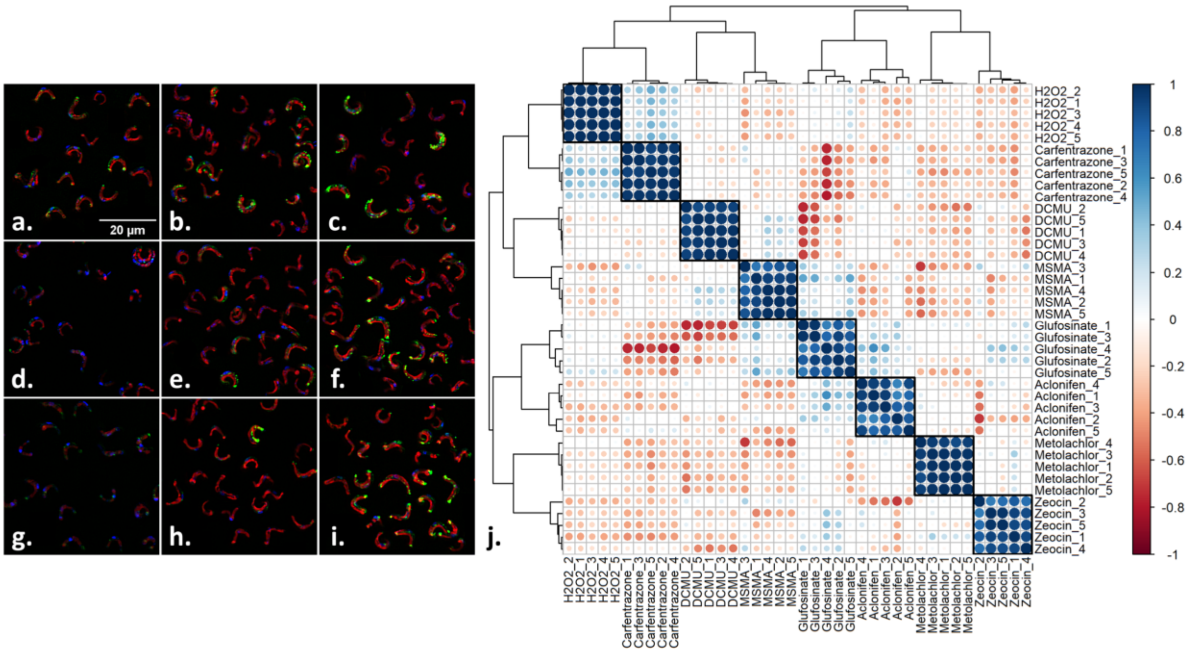

Figure 12: Phenotypic responses of reference chemicals compared to one another. (a.-i.) MACI labeling patterns in nine different treatment groups; (a.) Healthy Cells, (b.) Zeocin, (c.) Metolachlor, (d.) Carfentrazone, (e.) MSMA, (f.) Glufosinate, (g.) H_2O_2, (h.) DCMU, and (i.) Aclonifen treated cells. (j) Pearson correlation matrix across unique phenotypic responses. Chemical-treated samples are hierarchically clustered based on their Pearson coefficient in relation to the other chemical-treated samples; dendrograms and boxes represent individual clusters.

and Aclonifen had less correlation between replicates within their respective clusters in comparison to other chemical treatments, however, their overall correlations were still considerably high. Interestingly, some correlations between clusters could also been seen. For example, Carfentrazone and H_2O_2 clusters exhibited fairly high similarity to one another. This is not all that surprising, though, due to the similarity in the way each of these chemicals interact with algal cells and the stark visual similarities between their MACI labeling patterns (**Figure 12d.** and **12g.**, respectively). Additionally, DCMU and MSMA clusters, whose MoAs are both related to electron transport inhibition,[72,75] bore some slight similarity to one another. The Glufosinate and Aclonifen clusters were also slightly similar to one another, which is interesting as their MoAs aren't associated with one another, but may indicate some underlying similarities either in the way they interact with algal cells and/or in their initial downstream impacts. However, despite all of these intertreatment similarities, MACI was still sensitive to the subtle differences in their phenotypic responses, thus suggesting that this assay can be used to successfully predict compound-specific perturbations and discriminate between chemicals with unique MoAs.

Chemical MoAs can be identified based on phenotypic response using convolutional neural networks.

In addition to hierarchical clustering analysis, we also took a deep learning approach to analyze complex phenotypes and delineate chemicals by their MoA, using convolutional neural networks. CNNs are a type of artificial neural network, which are most notable for the way they process image data similarly to the visual cortex of the human brain.[85]

In CellProfiler Analyst, a CNN was trained on a small subset of randomly fetched cells from each treatment (~10.5% of cells from the entire experiment) using 50x50 neurons per layer. Based on the confusion matrix (**Figure 13**), the CNN model had some difficulty distinguishing certain mechanistic classes from one another, such as cells with membrane disruption vs DNA damage or cells with inhibited N_2 metabolism vs inhibited very-long-chain fatty acid synthesis. However, the CNN model was still able to predict the correct mechanistic class across training cells with moderately good classification at an accuracy of 75.07%. Once trained, the CNN model was used to score each cell in the experiment, based on its individual phenotype, with a predicted mechanistic class, and then calculate enrichment scores for each sample.

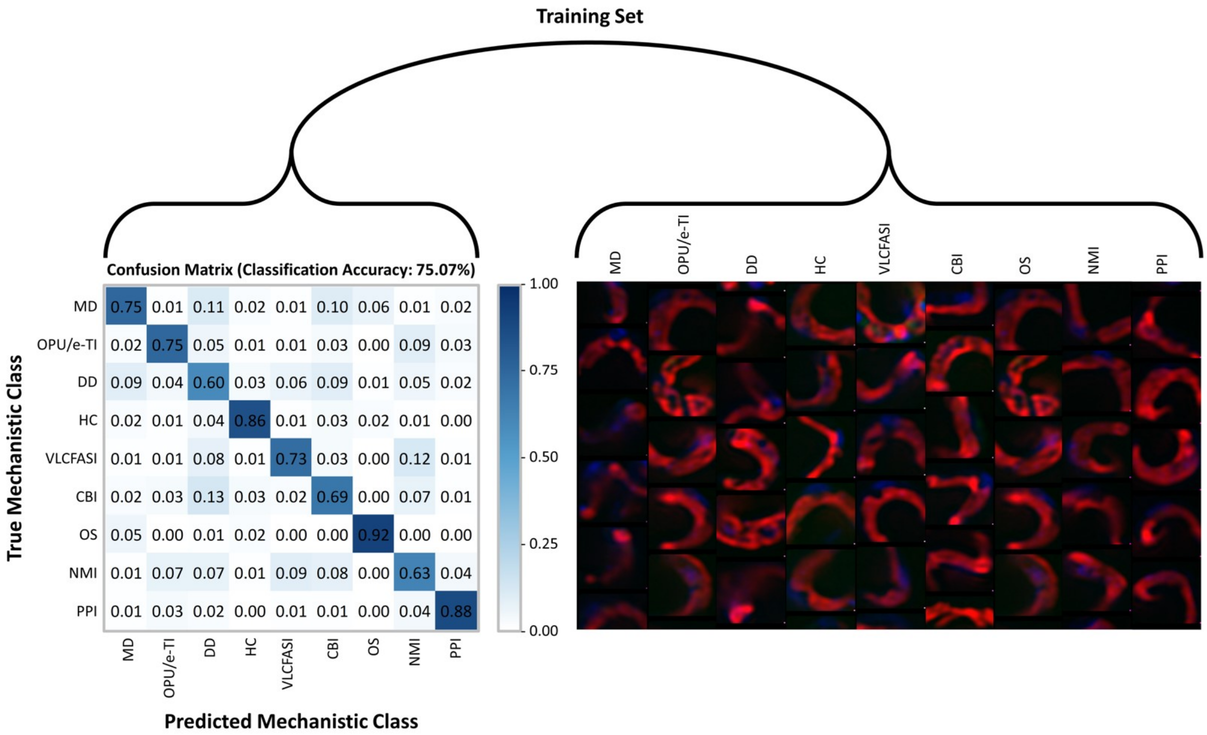

	MD	OPU/e-TI	DD	HC	VLCFASI	CBI	OS	NMI	PPI
MD	0.75	0.01	0.11	0.02	0.01	0.10	0.06	0.01	0.02
OPU/e-TI	0.02	0.75	0.05	0.01	0.01	0.03	0.00	0.09	0.03
DD	0.09	0.04	0.60	0.03	0.06	0.09	0.01	0.05	0.02
HC	0.02	0.01	0.04	0.86	0.01	0.03	0.02	0.01	0.00
VLCFASI	0.01	0.01	0.08	0.01	0.73	0.03	0.00	0.12	0.01
CBI	0.02	0.03	0.13	0.03	0.02	0.69	0.00	0.07	0.01
OS	0.05	0.00	0.01	0.02	0.00	0.00	0.92	0.00	0.00
NMI	0.01	0.07	0.07	0.01	0.09	0.08	0.00	0.63	0.04
PPI	0.01	0.03	0.02	0.00	0.01	0.01	0.00	0.04	0.88

Figure 13: Convolutional neural network construction. A small subset of randomly fetched cells in each treatment are fed into a convolutional neural network model. Based on the training data, this CNN model yields a classification accuracy of 75.07% at correctly classifying cells by their true mechanistic class.

Despite some confusion in the discrimination of mechanistic classes, the CNN model was still able to classify each treatment with the correct MoA. This is visualized in the heatmap of enrichment scores (**Figure 14**) where each treatment was significantly enriched in the appropriate mechanistic class. Based on these results, the deep learning approach reinforced the ability of MACI to separate chemicals by MoA. However, both deep learning and hierarchical clustering analyses proved to be robust and sensitive to subtle changes in complex phenotypes.

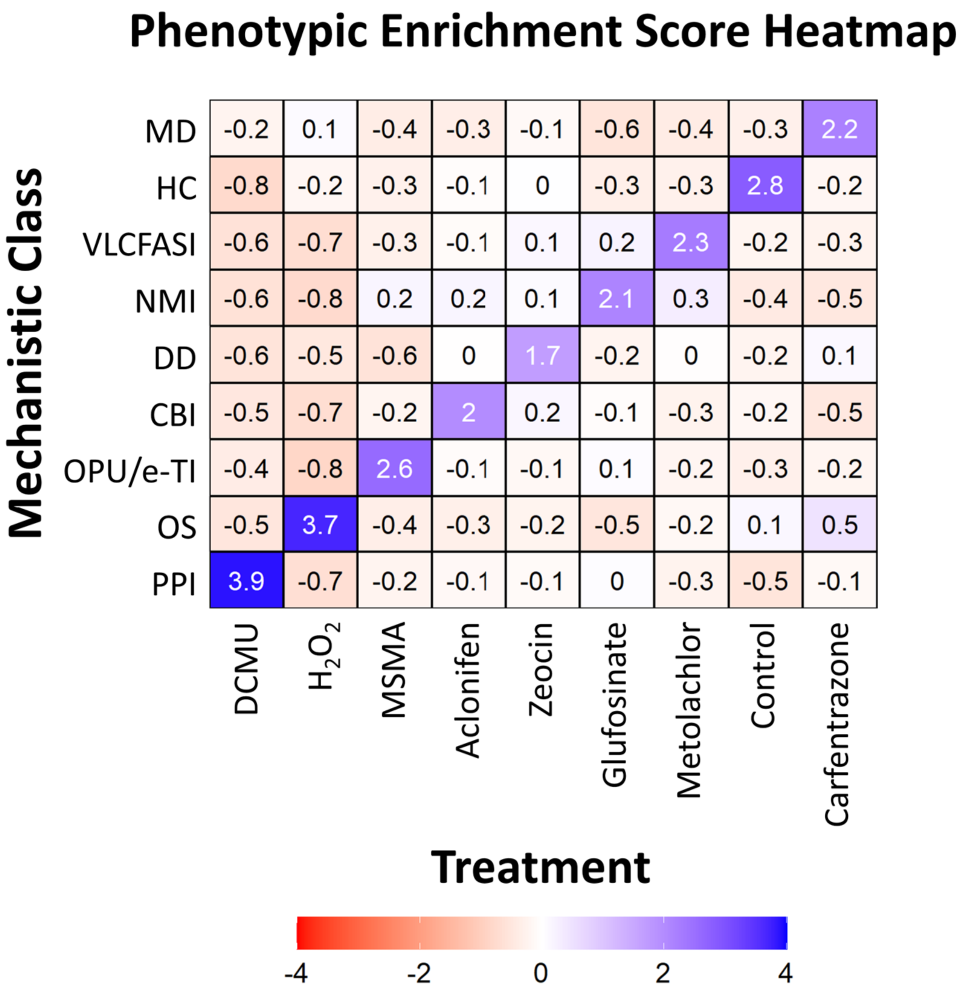

Phenotypic Enrichment Score Heatmap

	DCMU	H_2O_2	MSMA	Aclonifen	Zeocin	Glufosinate	Metolachlor	Control	Carfentrazone
MD	-0.2	0.1	-0.4	-0.3	-0.1	-0.6	-0.4	-0.3	2.2
HC	-0.8	-0.2	-0.3	-0.1	0	-0.3	-0.3	2.8	-0.2
VLCFASI	-0.6	-0.7	-0.3	-0.1	0.1	0.2	2.3	-0.2	-0.3
NMI	-0.6	-0.8	0.2	0.2	0.1	2.1	0.3	-0.4	-0.5
DD	-0.6	-0.5	-0.6	0	1.7	-0.2	0	-0.2	0.1
CBI	-0.5	-0.7	-0.2	2	0.2	-0.1	-0.3	-0.2	-0.5
OPU/e-TI	-0.4	-0.8	2.6	-0.1	-0.1	0.1	-0.2	-0.3	-0.2
OS	-0.5	3.7	-0.4	-0.3	-0.2	-0.5	-0.2	0.1	0.5
PPI	3.9	-0.7	-0.2	-0.1	-0.1	0	-0.3	-0.5	-0.1

Figure 14: Phenotypic enrichment score heatmap. The CNN model classifies each cell across the entire experiment with a predicted mechanistic class based on its phenotype. Enrichment scores for each mechanistic class are calculated in each sample. Heatmap values represent average treatment enrichment scores; white colored numbers represent significantly enriched mechanistic classes for respective treatments.

Complex phenotypic profiles are more efficient at predicting mechanisms of action rather than single interpretable features.

A majority of the morphological features used for phenotypic profiling are not interpretable on their own. Zernike moments, for example, measure specific aspects of an object's radial distribution,[86] and when multiple Zernike moments across multiple orders are combined together, they become powerful mathematical descriptors of that object's shape. Although they can be useful for reconstructing patterns and for detecting subtle changes in cell shape,[87] individual Zernike moments, by themselves, do not hold much intrinsic nor biological meaning. However, there are a select few of morphological features that do hold some biological relevance, such as those related to the intensity and quantity of fluorescence signals, which we can use to elucidate interesting biological phenomena. For example, measurements of integrated intensity, which is the sum of pixel intensity values over a ROI,[88] directly correlate to the number fluorophores in that ROI, and thus directly or indirectly measure relative levels of target biomolecular content. This kind of measurement has been used for analyzing endpoints related to changes in protein content[89] and for determining cell cycle stages based on the relative abundance of DNA content.[90,91] Another useful metric is quantifying the number of fluorescent objects within a single cell. For example, measuring the number of intracellular vesicles has been used to study endpoints related to the cellular uptake of micro/nano plastic particles[92] and for analyzing the intracellular trafficking of certain proteins.[93] In regard to *R. subcapitata*, three features that have relevance to algal physiology are the number of nuclei/cell, and the chloroplast and lipid droplet integrated intensities, which are related to chlorophyll and TAG content, respectively (**Supplementary Table S3**).

Often the phenotypic measurements that scientists are most interested in analyzing, such as the above-mentioned features, are not always the best predictors for characterizing the MoA of different compounds due to their lack of specificity. For example, 4 out of 8 treatments significantly increased chlorophyll content, while 4 out of 8 treatments also significantly increased the average number of nuclei/cell, in some cases to similar magnitudes while following similar trends to one another. TAG content was only significantly increased in Metolachlor treated cells, but most treatments did not elicit a significant change in TAG content. Furthermore, when using these three features in a hierarchical clustering analysis, based on Pearson correlation, the analysis was not sensitive enough to discriminate between chemical-specific perturbance (**Supplementary Figure S5**), as compared to the previous hierarchal clustering analysis using the entire profile (**Figure 11**). Ultimately, when conducting high-content phenotypic profiling, it is advised to evaluate changes in the entire profile, rather than changes in individual or select morphological features alone, as they do not hold enough information **that** can directly be linked to a specific MoA[58].

Applications of MACI and its advantages.

As the use of high-throughput phenotypic profiling assays become more popular, the MACI assay, in particular, could have several applications in different areas of research. Firstly, in the context of ecotoxicological research, MACI could be used to study the potential impacts of emerging contaminants and environmental chemicals on aquatic ecosystems by characterizing their cellular targets and identifying their phytotoxic MoAs. This could be especially useful if used alongside the Cell Painting assay with other environmentally relevant models like drosophila and rainbow trout gill cell lines to make cross-species comparisons that span multiple trophic levels. Additionally, in the context of environmental risk assessment, MACI could also be used to help prioritize which emerging contaminants and environmental chemicals require further evaluation. Secondly, MACI could be used as an *in vitro* model to drive developments in herbicide and agrochemical discovery. Green microalgae cells, like *R. subcapitata*, bear several similarities to the mesophyll cells of higher order terrestrial plants in terms of the cellular components/ constituents they contain, the environmental processes they carry out, and the evolutionarily conserved pathways and molecules they utilize.[94,95] Furthermore, since many herbicides and agrochemicals are delivered to plants via foliar application, MACI could be used for identifying cellular targets and determining MoAs of novel herbicides and agrochemicals. However, this technique may not be as useful for soil-based herbicides and agrochemicals.

Currently several high-throughput screening assays exist in addition to high-throughput phenotypic profiling, such as high-throughput transcriptomics and high-throughput proteomics. While both of these assays provide a rich molecular level understanding of chemical interactions, they can be extremely time-consuming, costly, and computationally expensive. In comparison, MACI, as an image-based profiling assay, provides the advantage of low cost and high speed, while still retaining a capacity for in-depth characterization and classification.[96,97] Additionally, assays which measure the differential expression of transcripts and proteins rely heavily on well-established annotations for those transcripts and proteins. This is an issue for most environmentally relevant organisms, like *R. subcapitata*, which have not been annotated to the extent with which human disease models have.[98] However, another advantage of MACI, and other image-based profiling assays, is that they only require comparisons to a library of reference chemicals with established MoAs in order to derive meaning from the phenotypic response of novel or unstudied chemicals[58]. Lastly, MACI provides the advantage of greater experimental precision as each individual cell, of which there can be up to 100,000's-1,000,000's in any given experiment, serves as an independent, technical measurement, thereby, also limiting the impact of measurement error.[99] Overall, based on the results described in this study, and the inherent advantages of this assay, MACI provides a quick and effective framework for characterizing complex phenotypes and compound-specific interactions which is suitable for predicting chemical MoAs in plant-type organisms.

2.5. Acknowledgement

This material is based on the work supported by the National Science Foundation, Center for Sustainable Nanotechnology (CSN; grant CHE-2001611). The CSN is part of the Centers for Chemical Innovation Program.

Chapter 3.

Predicting the phytotoxic mechanism of action of $LiCoO_2$ nanosheets using a novel multiplexed algal cytological imaging (MACI) assay and machine learning.

3.1. Abstract

Currently, there is a lack of knowledge of how complex metal oxide nanomaterials, like $LiCoO_2$ (LCO) nanosheets, interact with eukaryotic green algae. Previously, LCO was reported to cause a number of physiological impacts to *R. subcapitata* including endpoints related to growth, reproduction, pigment & lipid biosynthesis, and carbon biomass assimilation. Furthermore, LCO was proven to physically enter the cells, thus indicating the possibility for it to directly interact with key subcellular components. However, the mechanisms through which LCO interacts with these key subcellular components is still unknown. This chapter assesses the interactions of LCO at the biointerface of *R. subcapitata* using the novel multiplexed algal cytological imaging (MACI) assay, described in the previous chapter, and machine learning in order to predict the phytotoxic mechanism of action (MoA) of LCO. Algal cells were exposed to varying concentrations of LCO, and their phenotypic profiles were compared to that of cells treated with reference chemicals which had already established MoAs. Hierarchical clustering and machine learning analyses indicated photosynthetic electron transport to be the most probable phytotoxic MoA of LCO. Additionally,

single-cell chlorophyll fluorescence results demonstrated an increase in irreversibly oxidized photosystem II proteins. Lastly, LCO-treated cells were observed to have less nuclei/cell and less DNA content/nucleus when compared to non-treated cell controls.

3.2. Introduction

As the number of engineered nanomaterials found in the environment and commerce expands, understanding the breadth of their environmental consequences is a challenge we currently face. In particular, a class of nanomaterials we need more toxicological data on are complex metal oxide nanomaterials, like $LiCoO_2$ (LCO) nanosheets due to their high volume of production and presence in commerce.[4] LCO is one of the most commonly used cathode materials in rechargeable Li-ion batteries[1] and can be found in a multitude of consumer electronics from computers and smart phones to high-end electric vehicles. As such, the annual production rate for LCO has skyrocketed to levels of environmental significance in recent years.[4] What makes this matter particularly concerning, however, is that there is little to no infrastructure for recycling or for properly disposing of LIB's, nor is there any economic incentive to do so as it is cheaper to simply manufacture new battery materials.[4] For example, it is currently estimated that less than 5% of all LIB's are being recycled, with the rest ending up in landfills or being disposed of in other mean of un-sustainable storage.[6] As a result, this means that there is a high probability for LCO to be unintendedly released into the environment, thus posing an ecological risk. And what exacerbates this risk is that LCO contains high-valence metals with unique catalytic properties, high reactivity, and known inherent toxicity.[7,3] Thus, understanding the impacts of LCO to a wide diversity of environmentally relevant organisms across multiple trophic levels is of paramount importance. Current research has been done to assess LCO's toxicological impacts and mechanism of action

(MoA) in higher animal-type organisms. For example, Curtis et al., 2022 has reported LCO to cause a differential expression in electron transport and energy metabolism related genes across different fish and invertebrate species. Furthermore, Niemuth et al., 2020 has reported LCO to participate in redox reactions and alter the redox state of and Fe-S proteins, which are important for electron transport. However, our understanding of LCO's impacts to plant-type organisms is still limited.

In the first chapter, LCO was reported to cause a number of physiological impacts to *Raphidocelis subcapitata*, such as reduced growth, altered pigment biosynthesis, and impaired photosynthetic productivity.[101] Furthermore, LCO nanoparticles were proven to physically enter the algal cells, thus implying that they undergo direct interactions with key subcellular compartments.[101] However, our understanding of the mechanisms governing these consequences is still unclear. Given that photosynthesis was impacted in algae and its reverse reaction, respiration, has also been reportedly impacted in higher animal species,[100] it's likely that they may experience similar mechanistic disturbances. For example, key photosynthetic proteins like photosystem II (PSII), which facilitate electron flow in chloroplasts, could be impacted.

In order to assess the interactions of LCO at the biointerface of algal cells, a multiplexed algal cytological imaging (MACI) assay in combination with data mining and machine learning techniques can be used. MACI, as described in Chapter 2, is a type of high-throughput phenotypic profiling assay which involves the use of fluorescence cytochemistry to visualize multiple subcellular structures within the cell, and automated high-content fluorescence imaging to take hundreds of snapshots of their morphology in a consistent manner. In general, high-content phenotypic profiling works off the principal that the morphology of a cell is very sensitive to environmental cues[56] and that subtle, yet reproducible, alterations to subsets of morphological features can be used as a framework to characterize compound-specific interactions and predict MoAs of novel compounds when comparing their phenotypic profiles to that of compounds with established MoAs.[58] Additionally, image-based profiling assays provide the advantage of speed and cost effectiveness when compared to transcriptomic- and proteomic-based profiling assays.[96,97] However, MACI, in the context of eco- and phytotoxicological research, provides an additional benefit compared to other mainstream high-throughput phenotypic profiling assays, like Cell Painting,[59] in that it relies on the fluorescent labeling of subcellular structures that are unique to the architecture of algal cells which may more accurately characterize MoAs in plant-type species.

In this chapter, *R. subcapitata* cells were exposed to LCO for 24 hours, and MACI was used to characterize subcellular changes in their phenotype with the goal of understanding LCO-algal interactions. Their phenotypic profile was also compared to several reference compounds with established MoAs to predict the phytotoxic MoA of LCO. These reference compounds were chosen to represent MoAs that have been reported for other nanomaterials like membrane disruption,[40] DNA damage,[102] and more. The similarities between LCO and reference compound profiles were evaluated using hierarchical clustering based on Euclidean distance. An additional deep learning convolutional neural network (CNN) approach was also used to characterize the MoA experienced in individual cells as a means to predict LCO's phytotoxic MoA.

3.3. Materials and Methods

Algal Cell Culture.

A stock culture of *R. subcapitata*, inoculated at 1×10^5 Cells·mL^{-1}, was grown in a 1 L Erlenmeyer flask and cultured in OECD 201 media [21]. Cells were illuminated continuously with a full spectrum T8 light bulb at a photon flux of 70 μE·m^{-2}·s^{-1}. The stock culture was mixed with an orbital shaker at a speed of 111 rpm.

Exposure Setup.

This exposure was done to assess predict the phytotoxic MoA of LCO on *R. subcapitata* by comparing changes in the complex phenotype of LCO-treated cells to that of reference chemicals with established MoAs after 24 hours of exposure. An additional LCO exposure was done at 48 hours to better evaluate physiological endpoints such as nucleation state. Algae were exposed to one of four LCO concentrations or untreated control (0 μg·mL^{-1}, 0.01 μg·mL^{-1}, 0.1 μg·mL^{-1}, 1 μg·mL^{-1}, & 10 μg·mL^{-1} LCO), an ion control that contained the concentration of lithium and cobalt ions that would be present in the algae media containing 10 μg·mL^{-1} of LCO after 24 or 48 hours, depending on the exposure duration. In each treatment, 900 μL aliquots of algal stock culture were seeded into individual 1.5 mL microcentrifuge tubes after cells were growing exponentially. A stock suspension of LCO was constituted at 100 μg·mL^{-1} in OECD 201 media. For this study, the OECD 201 media was made to be deficient in EDTA in order to prevent the mitigation of any metal-induced stress. This suspension was sonicated for 25 minutes before the addition to respective samples to break up any aggregated nanoparticles. Additionally, an ion solution made from LiOH and $CoCl_2\cdot H_2O$, also constituted the OECD 201 media, was made at 10X the concentration of ion dissolution of 10 μg·mL^{-1} of LCO after 24 and 48 hours, depending on the exposure duration. For each treatment, OECD 201 media, LCO suspension, or 10X ion solution was added to each 900 μL cell suspension at a final volume of 1 mL. The samples were then placed under full spectrum illumination, with tube lids open, at a photon flux of 70 μE·m^{-2}

$\cdot s^{-1}$ for 24 hours. The 24 hour exposure duration was chosen for MoA prediction as this timepoint has been shown to better delineate initial phenotypic impacts[61], while the 48 hour exposure duration was chosen to examine physiological endpoints.

Single-Cell Chlorophyll Fluorescence.

At the conclusion of these exposures, a 50 μL aliquot from each sample was plated in to a well of a glass bottom 384 well plate (Cellvis, P384W-1.5H-N) and spun gently at 600RPM for 1 minute to concentrate cells at the bottom of the well. Cells were not stained nor fixed with glutaraldehyde for this assay as to prevent interference with raw fluorescence. Cells were then dark adapted for 30 min to ensure PSII centers were in an open, or oxidized, state before imaging with an ImageXpress Micro XLS High-Content Screening System. For image acquisition, cells were visualized using a Cy 5 filter (ex/em: 628/692) in a manner similar to that of a PAM Fluorometer, such that cells are exposed to a low intensity light beam followed by a saturating light beam to measure the minimal (F_0) and maximal (F_m) chlorophyll fluorescence, respectively (**Figure 15**) using the fluorescence cytochemistry parameters in **Table 4**. After acquiring images, bioimage analysis was used to measure the respective fluorescence intensities. Using the "mean_integrated_intensity" values for F_0 and F_m, the variable fluorescence (F_v) and quantum efficiency of PSII (F_v/F_m) of individual cells were calculated using the

following equation:

$$\frac{F_v}{F_m} = \frac{F_m - F_0}{F_m} \quad \text{……………………………………………..(6)}$$

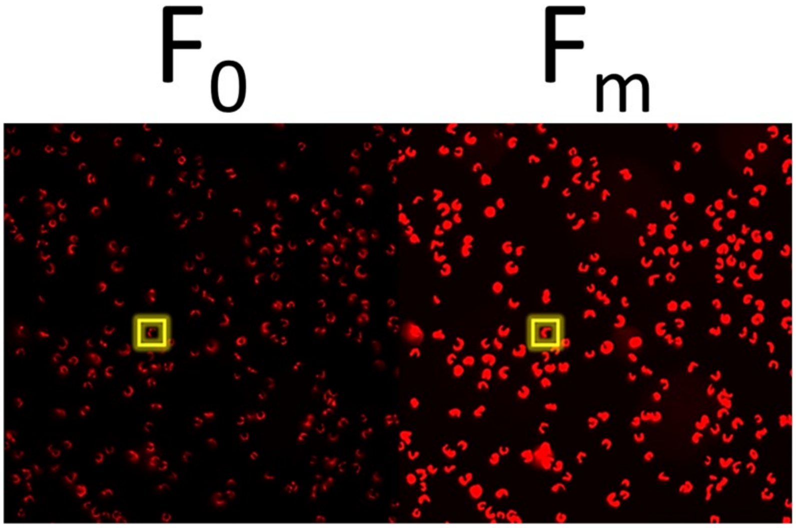

Figure 15: Representative fluorescence micrograph of single cells at an F_0 and F_m state, respectively.

Table 4: Single-Cell Chlorophyll Fluorescence Cytochemistry Parameters

Intensity	**Channel**	**Excitation (nm)**	**Emission (nm)**	**Exposure Time (nm)**
Minimal (F0)	Cy 5	628/40	692/40	35 ms
Maximal (Fm)	Cy5	628/40	692/40	270 ms

Multiplexed Algal Cytological Imaging (MACI) Assay.

The MACI assay was carried out as using methods described in Chapter 2. At the conclusion of the exposure, 905 µL aliquots from each sample were transferred to sterile 1.5 mL microcentrifuge tubes. Commercially available fluorescent probes were used to stain nuclei and lipid droplets using NucBlue (Thermo Fisher, R37605) and BODIPY 505/515 (Thermo Fisher, D3921), respectively, and glutaraldehyde were used to fix the algal cells. Reagent quantities, listed in **Table 2**, were added to each cell suspension at a final reaction volume of 1 mL. After adding reagents, all reactions were incubated overnight, at 4 °C to minimize enzymatic degradation and maintain the integrity of the subcellular structures. After incubating reactions, cells were centrifuged at 4000 x g for 5 min, washed 2x with 1X Phosphate Buffered Saline (PBS), and resuspended in PBS. Cells from each sample were loaded into a well of a glass bottom 384 well plate (Cellvis, P384W-1.5H-N) at a seeding density of ~2 $\times 10^3$ cells$\cdot$mm^{-2} for optimal distribution of cells across the well surface. After loading cells, the well plate was then spun gently at 600RPM for 1 minute to concentrate cells at the bottom of the well. Images were acquired at 9 sites per well with an ImageXpress Micro XLS High-Content Screening System with a 60X Plan Fluor 0.85 NA air immersion objective (Molecular Devices, 1-6300-0414), using the fluorescent channels described in **Table 3**. To enhance image contrast and resolution, the digital confocal feature was used during image acquisition. For representative cell images with higher resolution, some images were also acquired with a 100X CFI L PLAN EPI CC 0.85 NA air immersion objective (Molecular Devices, 1-6300-0419).

Bioimage Analysis.

After acquiring images CellProfiler,[29] was used for image pre-processing, object segmentation, and morphological feature extraction at the resolution of individual cells. Morphological features related to area, shape, intensity, and granularity of each subcellular structure were extracted, in addition to cytoplasmic intensity features to add more measurements for comparing the phenotypic profiles of LCO and reference chemical treatments, which were run on separate plates. These data were exported to a local SQLite database file and were then extracted using the RSQLite package in R.[78]

Phenotypic Profiling - Fingerprint Analysis.

Phenotypic response data was analyzed using the methods described in Chapter 2. The data was firstly processed by aggregating single-cell morphological feature measurements to per-image and then per-well values, which was done by taking the cell and image means, respectively. Secondly, well data from each compound and dose were then normalized to the non-treated cell control by computing a Z-score. In order to verify whether LCO elicited a change to the entire phenotypic profile of treated cells, a partial least squares-discriminant analysis (PLS-DA) was performed in R using the mixOmics package.[79] Before feeding phenotypic response data into the PLS-DA models, an ANOVA was performed across all features for each refence chemical to remove any non-informative features with little variance (p-values > 0.05). Lastly, factor analysis was used to further reduce the dimensionality of phenotypic data vectors, and the fingerprints were subsequently compared to one another using hierarchical clustering based on Euclidean distance in R.

Phenotypic Profiling - Convolutional Neural Networks.

In addition to fingerprint analysis, a CNN was also trained on a small subset of reference compound treated cells (~9.3%) using the classifier module on CellProfiler Analyst (Ver 3.0).[80] A separate bin was created for each reference chemical and the non-treated cell control in the classifier module, where around 1000 randomly fetched cells from each treatment were placed in each respective bin. For the non-treated cell control, cells form the reference chemical exposure and LCO exposure were both used to account for plate-to-plate and run-to-run variations. After training the CNN, it was used to score the entire experiment by classifying individual cells into predicted mechanistic classes, and computing enrichment scores for each sample as the logit area under the receiver operating characteristic curve. An ANOVA and a Tukey post-hoc test was used to evaluate the significance of predicted mechanistic class enrichments for each treatment.

Statistical Analysis.

All statistical analyses were performed using R Studio [30,31]. A Shapiro-Wilk test was used to verify normal distribution and a One-Way ANOVA was used to compare variance among group means, while a Tukey post-hoc test was used for multiple comparisons. In each analysis, significant differences were determined with a 95% confidence interval.

3.4. Results and Discussion

LCO significantly alters algal cell morphology after 24 hours.

After exposing *R. subcapitata* with LCO for 24 hours, the cells were stained and imaged using the MACI protocol (**Figure 16a**). In the representative fluorescence micrograph, the LCO-treated cells appear to be larger compared to the control cell, and also appear to have distinct levels of chlorophyll, TAG, and DNA content, which visually support the claim that LCO has an impact on cell morphology. A CellProfiler pipeline was used to convert the high-content image data into quantitative data where 570 unique, unbiased, morphological features of individual cells were used to generate phenotypic fingerprints of molecular interaction. In order to quantitatively verify if LCO treatment significantly alters algal cell morphology, a PLS-DA was used to analyze subtle changes in the complex phenotypic profile of LCO-treated cells with increasing concentration. Based on the PLS-DA response plot (**Figure 16b**), LCO-treated cells display a significant separation between response groups, thereby indicating that LCO does elicit a significant, and measurable, change to cell morphology after 24 hours. Based on X-variate data, a significant

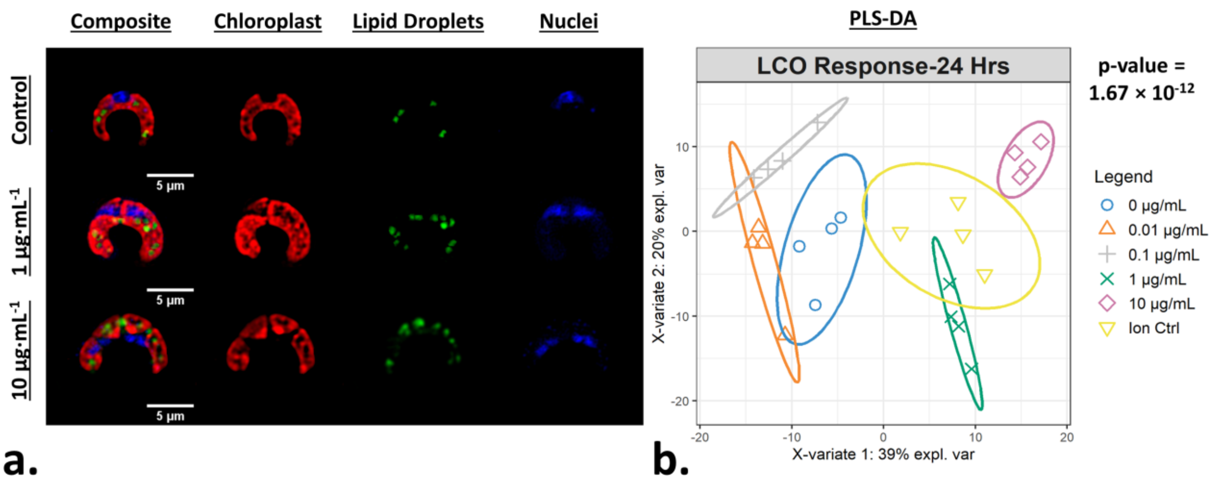

Figure 16: Phenotypic responses of algal cells when exposed to LCO. (a.) Representative fluorescence micrograph of MACI labeling patterns in treated and non-treated algal cells. (b.) A PLS-DA response plot graphically describes the change across complex morphological feature data with increasing concentration of LCO; ellipses represent 95% confidence intervals and p-values represent ANOVA statistics across the 1st latent variable between response groups.

separation from the control group can be seen at starting at the 0.1 ug·mL^{-1} response group. Here, the ion control response group also exhibited a significant separation from the control group. However, the ion control response group, which represents the amount of Li^+ and Co^{2+} ions released from 10 ug·mL^{-1} of LCO after 24 hours, was also significantly different form the 10 ug·mL^{-1} response group. Interestingly, this data suggests that while the ions do have somewhat of an impact on cell morphology, they are separate from nano-specific impacts.

Phenotypic profiles of LCO-treated cells compared to reference chemical-treated cells.

In order to predict the phytotoxic MoA of LCO, the phenotypic profiles of LCO-treated cells were compared to reference chemical-treated cells with known MoAs. For this purpose, the 10 µM reference chemical data was compared to the 1 ug·mL^{-1} LCO data, which is around 10 µM of LCO, to compare responses of similar concentrations.

After constructing the phenotypic fingerprints, an ANOVA was used to identify individual features that carry little information, which were removed from the analysis given a p-value > 0.05. Additionally, factor analysis was used to further reduce the dimensionality of the phenotypic data vectors down to 7 eigen features/factors in order to minimize redundant measurements while preserving variance. The phenotypic fingerprints across all replicates for each reference chemical and LCO treatment were hierarchically clustered based on Euclidean distance (**Figure 17**). Euclidean distance is a data mining technique that measures how far apart two points are in a high-dimensional feature space,[81] and can be calculated as the square root of the sum of squares between two vectors.[103]

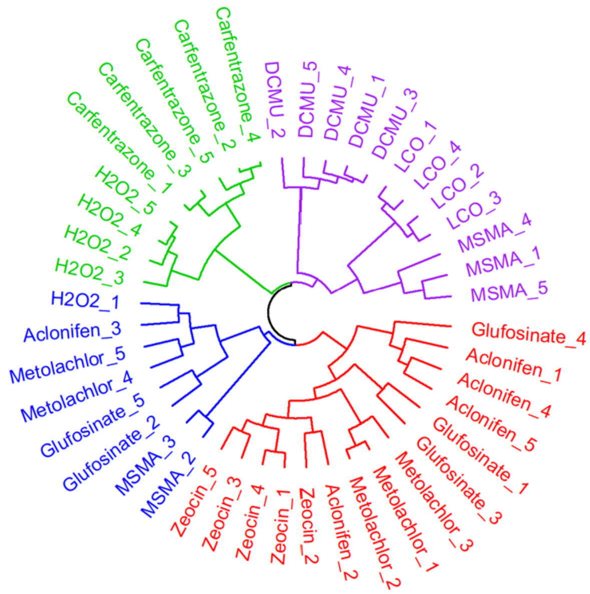

Figure 17: Dendrogram of hierarchically clustered LCO treated samples compared to reference chemical threated samples. Branches represent relative Euclidean distances between samples and nearest neighboring samples indicate the most similar phenotypic profiles to one-another.

The hierarchical clustering analysis was able to identify four main clusters. LCO-treated samples were clustered with DMCU and three of the MSMA-treated samples, thus indicating that their phenotypic profiles are most similar to one another. The MoAs of DMCU and MSMA are both related to electron transport inhibition in the chloroplast and mitochondrion, respectively.[72,75] Based on the results of the hierarchical clustering analysis, we can deduce that the probable MoA of LCO is also likely related to electron transport inhibition. This would makes sense as LCO tends to target proteins and pathways that are involved in transport of electrons.[13,100]

Predicting the MoA of individual LCO-treated cells using convolutional neural networks.

In addition to the hierarchical clustering analysis, a convolutional neural network was also used to classify individual LCO-treated cells into mechanistic classes. In CellProfiler Analyst, a CNN was trained on a small subset of randomly fetched cells from each treatment (~9.3% of cells from the combined LCO and reference chemical exposures) using 50x50 neurons per layer. For the healthy cell class, the CNN was trained on cells form the non-treated cell controls of both the LCO and reference chemical exposures as a means to account for variations due to separate plates and separate runs. Based on the confusion matrix (**Figure 18**), the CNN model was slightly less accurate at predicting the true mechanistic classes of cells compared to the CNN model in Chapter 2 (**Figure 13**), however it was still able to predict the correct mechanistic class across training cells with a moderately good classification accuracy of 73.82%. Once trained, the CNN model was used to score each cell in the LCO exposure, based on its individual phenotype, with a predicted mechanistic class, and then calculate enrichment scores for each sample.

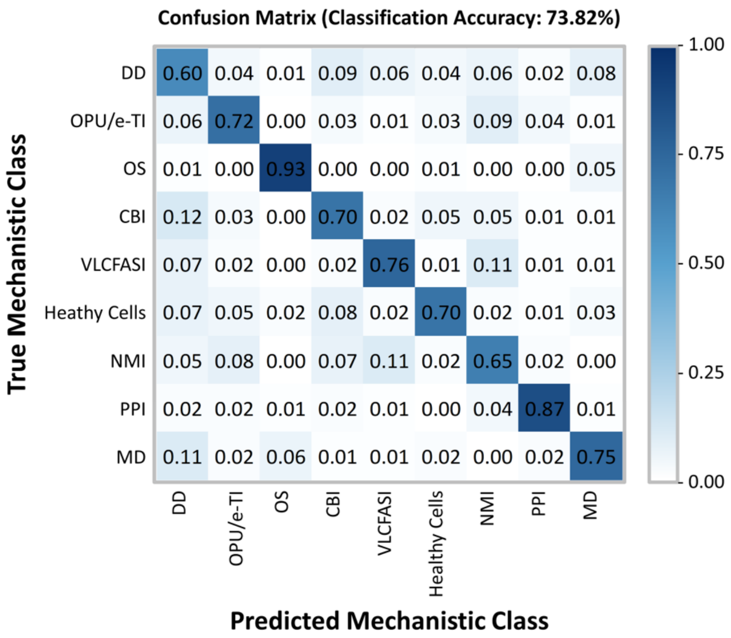

	DD	OPU/e-TI	OS	CBI	VLCFASI	Healthy Cells	NMI	PPI	MD
DD	0.60	0.04	0.01	0.09	0.06	0.04	0.06	0.02	0.08
OPU/e-TI	0.06	0.72	0.00	0.03	0.01	0.03	0.09	0.04	0.01
OS	0.01	0.00	0.93	0.00	0.00	0.01	0.00	0.00	0.05
CBI	0.12	0.03	0.00	0.70	0.02	0.05	0.05	0.01	0.01
VLCFASI	0.07	0.02	0.00	0.02	0.76	0.01	0.11	0.01	0.01
Heathy Cells	0.07	0.05	0.02	0.08	0.02	0.70	0.02	0.01	0.03
NMI	0.05	0.08	0.00	0.07	0.11	0.02	0.65	0.02	0.00
PPI	0.02	0.02	0.01	0.02	0.01	0.00	0.04	0.87	0.01
MD	0.11	0.02	0.06	0.01	0.01	0.02	0.00	0.02	0.75

Figure 18: Convolutional neural network construction. A small subset of randomly fetched cells in each treatment from the reference chemical and LCO exposures were fed into a convolutional neural network model. Based on the training data, this CNN model yields a classification accuracy of 73.82% at correctly classifying cells by their true mechanistic class.

The average enrichment scores for the LCO exposure are visualized in a heatmap (**Figure 19**) where values with asterisks (*) represent the mechanistic classes which are significantly enriched in each treatment when compared to the control. Based on these results, the CNN model predicted PSII photochemistry inhibition, or photosynthetic electron transport, as the most probable MoA of LCO with the highest and most significantly enriched scores. This was most notable in the 1 μg·mL^{-1} and ion control treatments. These treatments also obtained high enrichment scores in the oxidative phosphorylation uncoupler/mitochondrial electron transport inhibition mechanistic class; however, the scores were not significantly different from the control due to larger deviations in the enrichment data. This data coincides with the hierarchical clustering data (**Figure 17**) in that electron transport inhibition in general appears to be the most probable phytotoxic MoA of LCO, but the CNN data suggests that this disturbance is more prevalent in the photosynthetic pathway.

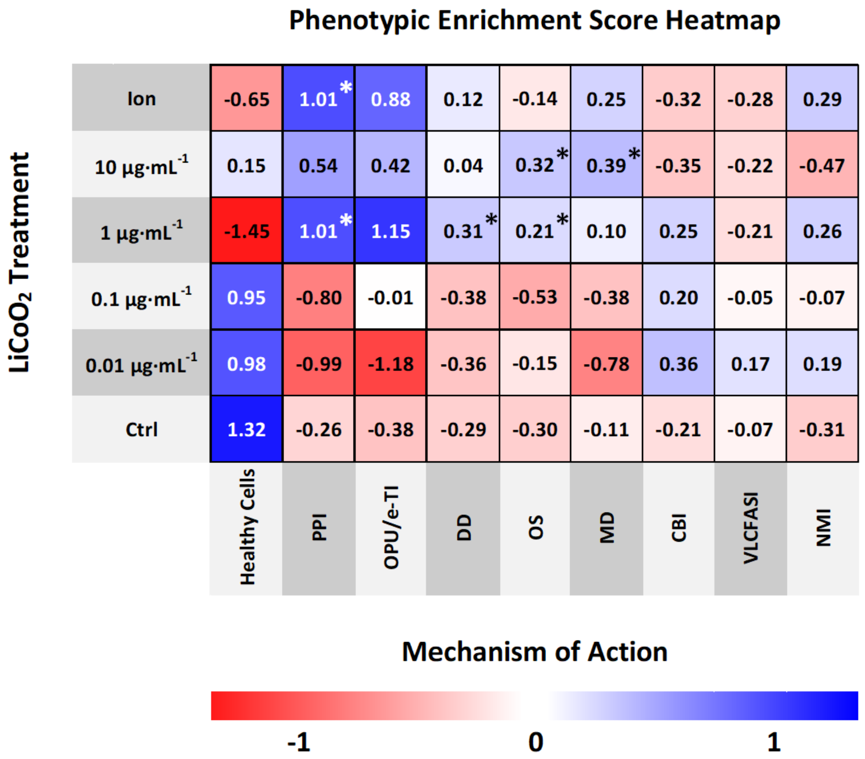

	Healthy Cells	PPI	OPU/e-TI	DD	OS	MD	CBI	VLCFASI	NMI
Ion	-0.65	1.01*	0.88	0.12	-0.14	0.25	-0.32	-0.28	0.29
10 µg·mL^{-1}	0.15	0.54	0.42	0.04	0.32*	0.39*	-0.35	-0.22	-0.47
1 µg·mL^{-1}	-1.45	1.01*	1.15	0.31*	0.21*	0.10	0.25	-0.21	0.26
0.1 µg·mL^{-1}	0.95	-0.80	-0.01	-0.38	-0.53	-0.38	0.20	-0.05	-0.07
0.01 µg·mL^{-1}	0.98	-0.99	-1.18	-0.36	-0.15	-0.78	0.36	0.17	0.19
Ctrl	1.32	-0.26	-0.38	-0.29	-0.30	-0.11	-0.21	-0.07	-0.31

Figure 19: Phenotypic enrichment score heatmap. The CNN model classifies each cell across the entire LCO exposure with a predicted mechanistic class based on its phenotype. Enrichment scores for each mechanistic class are calculated in each sample. Heatmap values represent average treatment enrichment scores; values with asterisks (*) represent significantly enriched mechanistic classes compared to the control.

Part of the advantage of using a CNN classifier model for phenotypic profiling is the fact that it can identify rare objects,[80] or smaller subpopulations of cells, in an otherwise heterogeneous cell population, that have distinct mechanistic classes that may go undetected with other phenotypic profiling methods that average across all cells. Interestingly, based off the enrichment data, there were also three other significantly enriched mechanistic classes found in much smaller subpopulations of cells. In the 1 µg·mL^{-1} treatment, the DNA damage and oxidative stress mechanistic classes were also significantly enriched. Additionally, in the 10 µg·mL^{-1} treatment, the oxidative stress and membrane disruption mechanistic classes were significantly enriched. These results may make sense as these mechanistic classes were only enriched in the highest concentrations of LCO, which are inherently more likely to have more cells undergoing a cytotoxic shock in which disturbances such as DNA damage, membrane disruption, and high levels of oxidative stress are experienced. However, it is important to reiterate here that the main MoA experienced by these cells is still largely photosynthetic electron transport inhibition as the other mechanistic classed were only indicated in a small percentage of cells.

Chlorophyll fluorescence markers indicate that LCO alters the oxidation state of PSII proteins.

Chlorophyll fluorescence is a non-invasive way to determine relative amounts of chlorophyll content in plant-type organisms and to assess the overall efficiency of photochemistry.[104,105] Several methods currently exist to make these sorts of measurements; Pulse Amplitude Modulation (PAM) fluorometers, for example, are typically used to make these measurements in leaf tissue and algal cells. PAM's work by, first, exposing the sample to a pulse of low intensity light to get the minimal fluorescence, as most of the energy will enter photochemistry and only a small portion will be re-emitted as fluorescence signal. This is then followed by a pulse of saturating light to get the maximal fluorescence, which at this point, the PSII reaction centers will already be reduced and thus most of the excited energy will be re-emitted as fluorescence signal. In general, the minimal fluorescence is comparable to the levels of chlorophyll present in leaf and algal samples.[104] Furthermore, by taking the ratio of minimal and maximal fluorescence, the quantum efficiency of PSII can be calculated,[106] which is a good indicator of photochemistry efficiency.[107] Here, this same concept was applied using high-content fluorescence microscopy for algal cells, and with this tool, the relative chlorophyll levels and quantum efficiencies of PSII evaluated for individual cells.

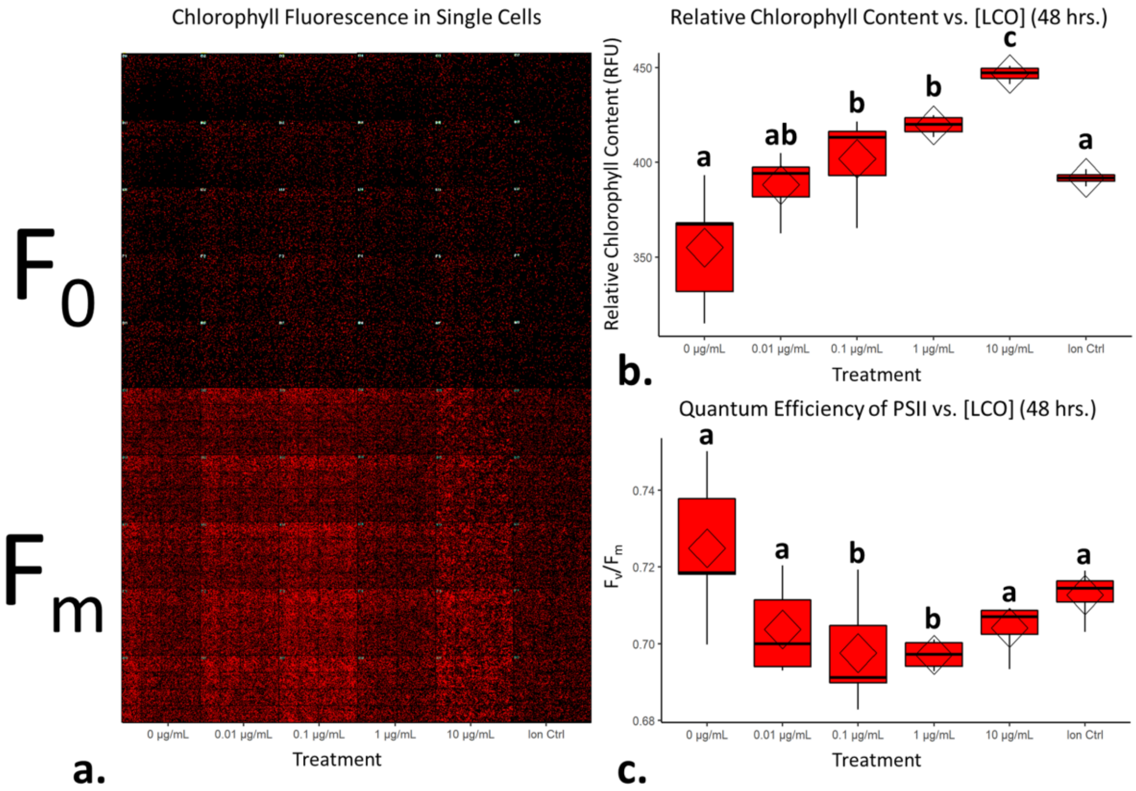

<u>Figure 20</u>: LCO significantly alters markers of chlorophyll fluorescence. (a.) Representative montage micrograph of algal cells across all treatments at a state of minimal and maximal fluorescence after 48 hours of exposure to LCO; (b.) Relative chlorophyll content after 48 hours of exposure to LCO; (c.) Quantum efficiency of PSII. Diamonds on boxplots represent treatment means and significant differences were determined using a one-way ANOVA with a Tukey post-hoc test for multiple comparisons; columns with different letters differ significantly ($p<0.05$).

Figure 20a displays measurements of single-cell chlorophyll fluorescence after being exposed to LCO for 48 hours; each red dot represents an individual cell. LCO treated cells had exhibited significant increases in chlorophyll content compared to that of the control (**Figure 20b**), which coincide with the results in Chapter 1 (**Figure 7e**). A quantum efficiency of PSII around 0.7 is considered healthy and/or normal for eukaryotic algal cells,[108,109] so based on the data in **Figure 20c**, even LCO treated cells are still within a normal range. Interesting, however, LCO treated cells exhibited a significant decrease in the quantum efficiency of PSII, compared to the control, in somewhat of a dose-dependent manner. In the context of the PSII biochemistry, this data would suggest that, in LCO treated cells, there is a higher fraction of damaged, or inactive, PSII reaction centers.[110] This type of disturbance is typically due to the irreversible oxidation of the D1 and D2 proteins in the PSII complex, usually following the production of $O_2^{\bullet -}$ and $OH^{\bullet}$ radicals.[111] These results, coincide with the hierarchical clustering (**Figure 17**) and CNN (**Figure 19**) analyses which predicted photosynthetic electron transport inhibition as the main phytotoxic MoA of LCO. Additionally, these results could help explain the reductions in the net production of carbon biomass reported in Chapter 1 (**Figure 5**).

LCO significantly impacts the nucleation state and DNA content after 48 hours.

In eukaryotic cells, the nucleus in an important subcellular compartment which houses the genetic material of the organism and is responsible for regulating gene expression and facilitating cellular division. Most green algae contain a unique multiple fission reproductive pattern in which one mother cell can divide into several daughter cells, depending on the environmental cues.[67] *R. subcapitata*, in particular, has the ability to divide into eight daughter cells,[66] and measuring the number of nuclei per cell, as well as the relative amount of DNA content per nucleus, can be used to describe instances of cell cycle disruption/arrest.[24, 67,70] After exposing cells to LCO for 48 hours, cells were stained with NucBlue, in order to fluorescently label the DNA content within the algae. A CellProfiler pipeline was used the count the number of nuclei/cell, as well as measure the integrated intensity of each nuclei, which was taken as relative DNA content. On average, LCO-treated sample contained a higher percentage of cells with only one nucleus when compared to the non-treated samples (**Figure 21a**). This affect increased in a dose-dependent manner, with significant differences from the control observed at 10 $\mu g \cdot mL^{-1}$ LCO and the ion control. The opposite trend was observed for cells with more than one nucleus (i.e. 2 & 4 nuclei), which also changed in a dose-dependent manner, with significant differences from the control observed at 10

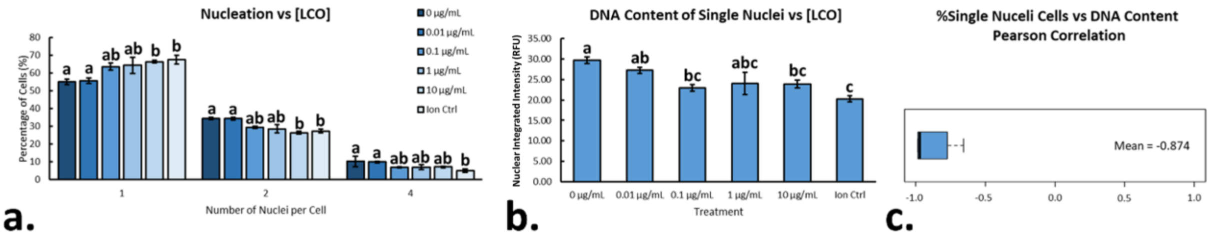

Figure 21: Nucleation state and relative DNA content in LCO-treated cells. (a.) Percentage of cells with 1, 2, or 4 nuclei after 48 hours of exposure to LCO; (b.) Relative DNA content of single nucleated cells; (c.) Pearson correlation between the percentage of single nucleated cells and their relative DNA content. Significant differences were determined using a one-way ANOVA with a Tukey post-hoc for multiple comparisons; columns with different letters differ significantly ($p<0.05$). Error bars represent SEM.

$\mu g \cdot mL^{-1}$ LCO and the ion control. Looking only at the cells with one nucleus, LCO-treated cells had, on average, a lesser relative amount of DNA content when compared to the non-treated control cell (**Figure 21b**). This was also observed in a dose-dependent manner, but with significant differences from the control at $0.1 \mu g \cdot mL^{-1}$ LCO, $10\ \mu g \cdot mL^{-1}$ LCO, and the ion control. Interestingly, when assessing the Pearson correlation between the two trends, a strong negative correlation was observed (**Figure 21c**). Together, these results indicate that, on average, LCO-treated cells exhibit an increased instance in the delay/arrest of cell cycle progression, specifically in the earlier stages of the cell cycle (stage 1/2) before first nuclear division.[70] Based on these results, it may explain the instances of increased growth inhibition and biovolume reported in Chapter 1 (**Figure 4a.-b.**). In this case, it may be possible that LCO had an impact on nuclear/cellular division through the impairment of photosynthetic electron transport.[112] These results are similar to that of DCMU treated cells, which, on average, had significantly less nuclei/cell when compared to non-treated control cells, and had appeared to have inhibited nuclear division (**Supplementary Table 3**). This would also be consistent with other photosynthetic organisms, like *Euglena gracilis*, in which similar impacts have been reported under impaired photosynthetic electron transport.[112]

3.5. Acknowledgement

This material is based on the work supported by the National Science Foundation, Center for Sustainable Nanotechnology (CSN; grant CHE-2001611). The CSN is part of the Centers for Chemical Innovation Program.

Conclusions

Summary of work.

This thesis aims to address the current gaps in our knowledge surrounding the toxicity of $LiCoO_2$ nanosheets to plant-type organisms. In this work, the phytotoxic impacts of LCO to the freshwater microalga, *Raphidocelis subcapitata*, were addressed.

The first chapter of this thesis addressed the general toxicological impacts of LCO, which were evaluated through analyzing different physiological endpoints relating to growth and energy production for algae cells. Following a LCO exposure lasting 48 hours, cells had exhibited a significant inhibition in growth at concentrations as low as 0.1 $\mu g \cdot mL^{-1}$, with an EC_{50} of 0.057 $\mu g \cdot mL^{-1}$, in addition to exhibiting significantly enlarged biovolumes at concentrations as low as 0.01 $\mu g \cdot mL^{-1}$. Furthermore, LCO-treated cells had produced significantly less carbon biomass, starting at 0.1 $\mu g \cdot mL^{-1}$, while significantly overproducing neutral lipid content, which is indicative of an interference with CO_2 assimilation chemistry and/or carbon partitioning. Additionally, relative chlorophyll content was also significantly increased, which may have been a compensatory effort to maximize light harvesting under an impaired photosynthetic apparatus. Lastly, enhanced darkfield hyperspectral imaging revealed physically internalize LCO deposits, thereby indicating the potential for LCO to directly interact with key subcellular components.

The second chapter addressed the need for more nontargeted, high-throughput profiling assays that can characterize biological activity, identify potency thresholds, and predict mechanisms of action (MoAs) for plant-type organisms like *R. subcapitata*, especially in the context of studying nanoparticle interactions. While other high-throughput screening assays already exist, such as high-throughput transcriptomics and high-throughput proteomics, these techniques can be expensive and time consuming, while relying on well-established transcript/protein annotations, which are lacking for most algae. In this chapter, methods were developed for a multiplexed cytological imaging (MACI) assay, based on the subcellular structures that are unique to microalgae, like *Raphidocelis subcapitata*. Several different herbicides and antibiotics with unique MoAs were exposed to *R. subcapitata* cells and MACI was used to characterize their cellular impacts by measuring subtle changes in the morphological features of treated cells. This assay offers a quick and effective framework for characterizing complex phenotypic responses to environmental chemicals, and emerging contaminants like engineered nanomaterials, that can be used for determining their MoAs and identifying their cellular targets in plant-type organisms.

In the third chapter, MACI and machine learning techniques were used to assess the interactions of LCO at the biointerface of *R. subcapitata* cells and to predict the phytotoxic MoA of LCO. Algal cells were exposed to varying concentrations of LCO, and their phenotypic profiles were compared to that of cells treated with reference chemicals with established MoAs. The described analyses predicted photosynthetic electron transport to be the most probable phytotoxic MoA of LCO, and single-cell chlorophyll fluorescence demonstrated an increase in irreversibly oxidized photosystem II proteins, thus fortifying the MACI assay prediction and coinciding with the impaired carbon biomass assimilation reported in the first chapter. Lastly, LCO-treated cells were observed to have less nuclei/cell and less DNA content/nucleus when compared to non-treated cell controls, which suggests an interference with cell cycle progression and complementing the growth inhibition and biovolume data reported in the first chapter.

Future directions.

While the toxicity of LCO to microalgae has been investigated in this work, more research should be done to address the impacts of LCO on terrestrial plants. For example, *Glycine max* would be a good model to use for phytotoxicity. Firstly, it has historically been used as a terrestrial model for toxicology due to its desirable characteristics such as its ability to be grown in laboratory environments, having good reproducibility within and across testing facilities, and its sensitivity to many toxic compounds.[113] Furthermore, *G. max* is also a very important crop that, as a leguminous plant, can fix atmospheric nitrogen through its microbial symbiotic relationship with the soil bacterium, rhizobium.[114] This, in part, would give us more information to the impacts of LCO on other environmental processes like nitrogen fixation and nitrogen assimilation. But also, its worldwide scale of cultivation and its major source of nutritional value (protein/oils/carbohydrates) make it a relevant organism to study.[115] Lastly, it would be useful to compare the impacts of LCO in *R. subcapitata* to *G. max* in order to verify elucidate any unifying mechanisms of phytotoxicity across species.

References Cited

1. Brog, J. P. *et al.* Characteristics and properties of nano - LiCoO 2 synthesized by pre - organized single source precursors : Li - ion diffusivity , electrochemistry and biological assessment. *J. Nanobiotechnology* 1–23 (2017). doi:10.1186/s12951-017-0292-3

2. Mizushima, K., Jones, P. C., Wiseman, P. J. & Goodenough, J. B. Li x CoO2 ($0<x\leqq1$): A New Cathode Material for Batteries of High Energy Density. *Elsevier* **15**, 425–428 (1982).

3. Nitta, N., Wu, F., Lee, J. T. & Yushin, G. Li-ion battery materials: present and future. *Biochem. Pharmacol.* **18**, 252–264 (2015).

4. Hamers, R. J. Energy storage materials as emerging nano-contaminants. *Chem. Res. Toxicol.* **33**, 1074–1081 (2020).

5. Keller, A. A. & Lazareva, A. Predicted Releases of Engineered Nanomaterials: From Global to Regional to Local. *Environ. Sci. Technol. Lett.* **1**, 65–70 (2013).

6. Kang, D. H. P., Chen, M. & Ogunseitan, O. A. Potential environmental and human health impacts of rechargeable lithium batteries in electronic waste. *Environ. Sci. Technol.* **47**, 5495–5503 (2013).

7. Lu, Z. *et al.* Electrochemical tuning of layered lithium transition metal oxides for improvement of oxygen evolution reaction. *Nat. Commun.* **5**, 1–7 (2014).

8. Bozich, J., Hang, M., Hamers, R. & Klaper, R. Core chemistry influences the toxicity of multicomponent metal oxide nanomaterials, lithium nickel manganese cobalt oxide, and lithium cobalt oxide to Daphnia magna. *Environ. Toxicol. Chem.* **36**, 2493–2502 (2017).

9. Melby, E. S. *et al.* Impact of lithiated cobalt oxide and phosphate nanoparticles on rainbow

trout gill epithelial cells. *Nanotoxicology* **12**, 1166–1181 (2018).

10. Niemuth, N. J. *et al.* Next-Generation Complex Metal Oxide Nanomaterials Negatively Impact Growth and Development in the Benthic Invertebrate Chironomus riparius upon Settling. *Environ. Sci. Technol.* **53**, 3860–3870 (2019).

11. Niemuth, N. J. *et al.* Energy Starvation in Daphnia magna from Exposure to a Lithium Cobalt Oxide Nanomaterial . *Chem. Res. Toxicol.* (2021). doi:10.1021/acs.chemrestox.1c00189

12. Mensch, A. C. *et al.* Subtoxic dose of lithium cobalt oxide nanosheets impacts critical molecular pathways in trout gill epithelial cells. *Environ. Sci. Nano* **7**, 3419–3430 (2020).

13. Niemuth, N. J. *et al.* Protein Fe-S Centers as a Molecular Target of Toxicity of a Complex Transition Metal Oxide Nanomaterial with Downstream Impacts on Metabolism and Growth. *Environ. Sci. Technol.* **54**, 15257–15266 (2020).

14. U.S. Environmental Protection Agency. Ecological Effects Test Guidelines OCSPP 850.4500: Algal Toxicity. Office of Chemical Safety and Pollution Prevention; Washington, D.C. (EPA-712C-006. *United States Environ. Prot. Agency* 26 (2012).

15. Murphy, L. THE ELECTRIFYING PROBLEM OF USED LITHIUM ION BATTERIES : RECOMMENDATIONS FOR LITHIUM ION BATTERY RECYCLING AND DISPOSAL. (2017).

16. Wang, F. *et al.* Effects of Nanoparticles on Algae: Adsorption, Distribution, Ecotoxicity and Fate. (2019). doi:10.3390/app9081534

17. Prasad, R. *et al.* Role of microalgae in global co2 sequestration: Physiological mechanism,

recent development, challenges, and future prospective. *MDPI* **13**, (2021).

18. Sayers, M. J., Fahnenstiel, G. L., Shuchman, R. A. & Bosse, K. R. A new method to estimate global freshwater phytoplankton carbon fixation using satellite remote sensing: initial results. *Int. J. Remote Sens.* **42**, 3708–3730 (2021).

19. Laudadio, E. D., Bennett, J. W., Green, C. M., Mason, S. E. & Hamers, R. J. Impact of Phosphate Adsorption on Complex Cobalt Oxide Nanoparticle Dispersibility in Aqueous Media. *Environ. Sci. Technol.* **52**, 10186–10195 (2018).

20. Laudadio, E. D., Ilani-Kashkouli, P., Green, C. M., Kabengi, N. J. & Hamers, R. J. Interaction of Phosphate with Lithium Cobalt Oxide Nanoparticles: A Combined Spectroscopic and Calorimetric Study. *Langmuir* **35**, 16640–16649 (2019).

21. OECD. Test No. 201: Freshwater Alga and Cyanobacteria, Growth Inhibition Test. Organization for Economic Cooperation and Development. OECD Guidelines for Testing of Chemicals, Section 2. OECD Publishing Service, Paris, France. (2011). doi:https://doi.org/10.1787/9789264069923

22. Ritz, C. & Strebig, J. C. Package ‘drc’: Analysis of Dose-Response Curves. *R Proj.* 149 (2016).

23. Borics, G. *et al.* Biovolume and surface area calculations for microalgae, using realistic 3D models. *Sci. Total Environ.* **773**, (2021).

24. Machado, M. D. & Soares, E. V. Reproductive cycle progression arrest and modification of cell morphology (shape and biovolume) in the alga Pseudokirchneriella subcapitata exposed to metolachlor. *Aquat. Toxicol.* **222**, 105449 (2020).

25. Esra Dökümcüoğlu, V. & Yılmaz, M. Assessment of Cell Counting Method Based on Image Processing for a Microalga Culture. *MedFAR* **3**, 75–81 (2020).

26. Machado, M. D. & Soares, E. V. Modification of cell volume and proliferative capacity of Pseudokirchneriella subcapitata cells exposed to metal stress. *Aquat. Toxicol.* **147**, 1–6 (2014).

27. Sun, J. & Liu, D. Geometric models for calculating cell biovolume and surface area for phytoplankton. *J. Plankton Res.* **25**, 1331–1346 (2003).

28. Bellou, S. & Aggelis, G. Biochemical activities in Chlorella sp. and Nannochloropsis salina during lipid and sugar synthesis in a lab-scale open pond simulating reactor. *J. Biotechnol.* **164**, 318–329 (2012).

29. Stirling, D. R. *et al.* CellProfiler 4: improvements in speed, utility and usability. *BMC Bioinformatics* **22**, 1–11 (2021).

30. R Core Team. R: A Language and Environment for Statistical Computing. (2019).

31. RStudio Team. RStudio: Integrated Development Environment for R. (2020).

32. Samimi, S., Maghsoudnia, N., Eftekhari, R. B. & Dorkoosh, F. *Lipid-Based Nanoparticles for Drug Delivery Systems*. *Characterization and Biology of Nanomaterials for Drug Delivery: Nanoscience and Nanotechnology in Drug Delivery* (Elsevier Inc., 2019). doi:10.1016/B978-0-12-814031-4.00003-9

33. Afshinnia, K. *et al.* Effect of nanomaterial and media physicochemical properties on Ag NM aggregation kinetics. *J. Colloid Interface Sci.* 1–31 (2019).

34. Hang, M. N. *et al.* Impact of Nanoscale Lithium Nickel Manganese Cobalt Oxide (NMC)

on the Bacterium Shewanella oneidensis MR-1. *Chem. Mater.* **28**, 1092–1100 (2016).

35. Antal, T. K., Krendeleva, T. E. & Tyystjärvi, E. Multiple regulatory mechanisms in the chloroplast of green algae: Relation to hydrogen production. *Photosynth. Res.* **125**, 357–381 (2015).

36. Johnson, X. & Alric, J. Central carbon metabolism and electron transport in chlamydomonas reinhardtii: Metabolic constraints for carbon partitioning between oil and starch. *Eukaryotic Cell* **12**, 776–793 (2013).

37. Harchouni, S., Field, B. & Menand, B. AC-202, a highly effective fluorophore for the visualization of lipid droplets in green algae and diatoms. *Biotechnol. Biofuels* **11**, 1–9 (2018).

38. Battah, M., El-Ayoty, Y., Abomohra, A. E. F., El-Ghany, S. A. & Esmael, A. Effect of Mn2+, Co2+ and H2O2 on biomass and lipids of the green microalga Chlorella vulgaris as a potential candidate for biodiesel production. *Ann. Microbiol.* **65**, 155–162 (2015).

39. Ischebeck, T., Krawczyk, H. E., Mullen, R. T., Dyer, J. M. & Chapman, K. D. Lipid droplets in plants and algae: Distribution, formation, turnover and function. *Semin. Cell Dev. Biol.* **108**, 82–93 (2020).

40. Malina, T. *et al.* Toxicity of graphene oxide against algae and cyanobacteria: Nanoblade-morphology-induced mechanical injury and self-protection mechanism. *Carbon N. Y.* **155**, 386–396 (2019).

41. Li, X. *et al.* Development of Protoporphyrinogen Oxidase as an Efficient Selection Marker for Agrobacterium tumefaciens-Mediated Transformation of Maize. *Plant Physiol.* **133**,

736–747 (2003).

42. Saxena, P. & Harish. Nanoecotoxicological Reports of Engineered Metal Oxide Nanoparticles on Algae. *Curr. Pollut. Reports* **4**, 128–142 (2018).

43. Vieira, E. M., Sarmento, H., Rocha, O. & Seleghim, M. H. R. Effects of diuron and carbofuran and their mixtures on the microalgae Raphidocelis subcapitata. *Ecotoxicol. Environ. Saf.* **142**, 312–321 (2017).

44. Yan, N. & Wang, W. X. Novel Imaging of Silver Nanoparticle Uptake by a Unicellular Alga and Trophic Transfer to Daphnia magna. *Environ. Sci. Technol.* **55**, 5143–5151 (2021).

45. Zhang, C., Chen, X., Chou, W. C. & Ho, S. H. Phytotoxic effect and molecular mechanism induced by nanodiamonds towards aquatic Chlorella pyrenoidosa by integrating regular and transcriptomic analyses. *Chemosphere* **270**, 129473 (2021).

46. Dai, Q. *et al.* Particle Targeting in Complex Biological Media. *Adv. Healthc. Mater.* **7**, 1–32 (2018).

47. Atamna, H., Walter, P. B. & Ames, B. N. The role of heme and iron-sulfur clusters in mitochondrial biogenesis, maintenance, and decay with age. *Arch. Biochem. Biophys.* **397**, 345–353 (2002).

48. Moura, I., Moura, J. J. G., Münck, E., Papaefthymiou, V. & LeGall, J. Evidence for the Formation of a CoFe3S4 Cluster in Desulfovibrio gigas Ferredoxin II. *J. Am. Chem. Soc.* **108**, 349–351 (1986).

49. Kaladharan, P., Pillai, V. K. & Balachandran, V. K. Inhibition of Primary Production As

Induced By Heavy Metal Ions on Phytoplankton Population Off Cochin. **37**, 51–54 (1990).

50. H.Kim, J.; J.Gibbs, H.; D.Howe, P.; Wood, M. Concise International Chemical Assessment Document 69: Cobalt and Inorganic Cobalt Compounds. *World Heal. Organ.* 1–93 (2006).

51. Horvatić, J., Peršić, V., Pavlić, Ž., Stjepanović, B. & Has-Schön, E. Toxicity of metals on the growth of Raphidocelis subcapitata and Chlorella kessleri using microplate bioassays. *Fresenius Environ. Bull.* **16**, 826–831 (2007).

52. El-Sheekh, M. M., El-Naggar, A. H., Osman, M. E. H. & El-Mazaly, E. Effect of cobalt on growth, pigments and the photosynthetic electron transport in Monoraphidium minutum and Nitzchia perminuta. *Brazilian J. Plant Physiol.* **15**, 159–166 (2003).

53. Kim, K. *et al.* Sulfolipid density dictates the extent of carbon nanodot interaction with chloroplast membranes. *Environ. Sci. Nano* **9**, 2691–2703 (2022).

54. Yaakob, M. A., Mohamed, R. M. S. R., Al-Gheethi, A., Ravishankar, G. A. & Ambati, R. R. Influence of nitrogen and phosphorus on microalgal growth, biomass, lipid, and fatty acid production: An overview. *Cells* **10**, 1–19 (2021).

55. Thomas, R. S. *et al.* The next generation blueprint of computational toxicology at the U.S. Environmental protection agency. *Toxicol. Sci.* **169**, 317–332 (2019).

56. States, C. *et al.* Multiplex cytological profiling assay to measure diverse. *PLoS One* **8**, 1–7 (2013).

57. Willis, C., Nyffeler, J. & Harrill, J. Phenotypic Profiling of Reference Chemicals across Biologically Diverse Cell Types Using the Cell Painting Assay. *SLAS Discov.* **25**, 755–769 (2020).

58. Svenningsen, E. B. & Poulsen, T. B. Bioorganic & Medicinal Chemistry Establishing cell painting in a smaller chemical biology lab – A report from the frontier. *Bioorg. Med. Chem.* **27**, 2609–2615 (2019).

59. Bray, M. *et al.* Cell Painting , a high-content image-based assay for morphological profiling using multiplexed fluorescent dyes. **11**, 1757–1774 (2016).

60. Hughes, R. E. *et al.* High-Content Phenotypic Profiling in Esophageal Adenocarcinoma Identifies Selectively Active Pharmacological Classes of Drugs for Repurposing and Chemical Starting Points for Novel Drug Discovery. *SLAS Discov.* **25**, 770–782 (2020).

61. Nyffeler, J. *et al.* Bioactivity screening of environmental chemicals using imaging-based high- throughput phenotypic profiling. *Toxicol. Appl. Pharmacol.* **389**, 114876 (2020).

62. Huovinen, M., Loikkanen, J., Naarala, J. & Vähäkangas, K. Toxicity of diuron in human cancer cells. *Toxicol. Vitr.* **29**, 1577–1586 (2015).

63. Magnusson, M., Heimann, K. & Negri, A. P. Comparative effects of herbicides on photosynthesis and growth of tropical estuarine microalgae. *Mar. Pollut. Bull.* **56**, 1545–1552 (2008).

64. Nohynek, G. J., Dufour, E. K. & Roberts, M. S. Nanotechnology, cosmetics and the skin: Is there a health risk? *Skin Pharmacol. Physiol.* **21**, 136–149 (2008).

65. Aruoja, V., Dubourguier, H. C., Kasemets, K. & Kahru, A. Toxicity of nanoparticles of CuO, ZnO and TiO2 to microalgae Pseudokirchneriella subcapitata. *Sci. Total Environ.* **407**, 1461–1468 (2009).

66. Yamagishi, T., Yamaguchi, H., Suzuki, S., Horie, Y. & Tatarazako, N. Cell reproductive

patterns in the green alga Pseudokirchneriella subcapitata (=Selenastrum capricornutum) and their variations under exposure to the typical toxicants potassium dichromate and 3,5-DCP. (2017). doi:10.1371/journal.pone.0171259

67. Zachleder, V. & Vítová, M. *The Physiology of Microalgae*. *The Physiology of Microalgae* (Springer Cham, 2016). doi:10.1007/978-3-319-24945-2

68. Roccuzzo, S. *et al.* Metabolic Insights Into Infochemicals Induced Colony Formation and Flocculation in Scenedesmus subspicatus Unraveled by Quantitative Proteomics. *Front. Microbiol.* **11**, 1–17 (2020).

69. Jakob, T., Schreiber, U., Kirchesch, V., Langner, U. & Wilhelm, C. Estimation of chlorophyll content and daily primary production of the major algal groups by means of multiwavelength-excitation PAM chlorophyll fluorometry: Performance and methodological limits. *Photosynth. Res.* **83**, 343–361 (2005).

70. Hlavová, M., Vítová, M., Bišová, K. & Zachleder, V. M. DNA Damage during G2 Phase Does Not Affect Cell Cycle Progression of the Green Alga Scenedesmus quadricauda. (2011). doi:10.1371/journal.pone.0019626

71. Almeida, A. C., Gomes, T., Langford, K., Thomas, K. V. & Tollefsen, K. E. Oxidative stress in the algae Chlamydomonas reinhardtii exposed to biocides. *Aquat. Toxicol.* **189**, 50–59 (2017).

72. Glauch, L. & Escher, B. I. The Combined Algae Test for the Evaluation of Mixture Toxicity in Environmental Samples. **39**, 2496–2508 (2020).

73. Nagai, T. Sensitivity differences among seven algal species to 12 herbicides with various

modes of action. *J. Pestic. Sci.* **44**, 225–232 (2019).

74. Geer, T. D., Kinley, C. M., Iwinski, K. J., Calomeni, A. J. & Rodgers, J. H. Comparative toxicity of sodium carbonate peroxyhydrate to freshwater organisms. *Ecotoxicol. Environ. Saf.* **132**, 202–211 (2016).

75. Dayan, F. E. & Zaccaro, M. L. de M. Chlorophyll fluorescence as a marker for herbicide mechanisms of action. *Pestic. Biochem. Physiol.* **102**, 189–197 (2012).

76. Čížková, M., Slavková, M., Vítová, M., Zachleder, V. & Bišová, K. Response of the green alga Chlamydomonas reinhardtii to the DNA damaging agent zeocin. *Cells* **8**, (2019).

77. Shapiro, H. M., Perlmutter, N. G. & Shapiro, H. M. A simple and highly efficient fixation method for Chrysochromulina polylepis (Prymnesiophytes) for analytical flow cytometry. *Cytometry* **44**, 126–132 (2001).

78. Müller, K., Wickham, H., James, D. A. & Falcon, S. RSQLite: SQLite Interface for R. (2023). doi:https://rsqlite.r-dbi.org, https://github.com/r-dbi/RSQLite.

79. Rohart, F., Gautier, B., Singh, A. & Lê Cao, K.-A. mixOmics: An R package for 'omics feature selection and multiple data integration. *PLoS Comput. Biol.* **13**, 1–14 (2017).

80. Stirling, D. R., Carpenter, A. E. & Cimini, B. A. CellProfiler Analyst 3.0: accessible data exploration and machine learning for image analysis. *Bioinformatics* **37**, 3992–3994 (2021).

81. Caicedo, J. C. *et al.* Data-analysis strategies for image-based cell profiling. *Nat. Methods* **14**, 849–863 (2017).

82. Lee, L. C., Liong, C. Y. & Jemain, A. A. Partial least squares-discriminant analysis (PLS-DA) for classification of high-dimensional (HD) data: A review of contemporary practice

strategies and knowledge gaps. *Analyst* **143**, 3526–3539 (2018).

83. Chandrasekaran, S. N., Ceulemans, H., Boyd, J. & Carpenter, A. E. Image- based profiling for drug discovery: due for a machine- learning upgrade? *Nat. Rev. Drug Discov.* **20**, (2021).

84. Young, D. W. *et al.* Integrating high-content screening and ligand-target prediction to identify mechanism of action. *Nat. Chem. Biol.* **4**, 59–68 (2008).

85. Dürr, O. & Sick, B. Single-cell phenotype classification using deep convolutional neural networks. *J. Biomol. Screen.* **21**, 998–1003 (2016).

86. Allen, P., Calcagni, A., Robson, A. G. & Claridge, E. Investigating the potential of Zernike polynomials to characterise spatial distribution of macular pigment. *PLoS One* **14**, 1–19 (2019).

87. Boland, M. V., Markey, M. K. & Murphy, R. F. Automated recognition of patterns characteristic of subcellular structures in fluorescence microscopy images. *Cytometry* **33**, 366–375 (1998).

88. Subramanian, G. & Vijaya, A. Iterative Intensity Integration Technique (IIIT) for contouring reflective surfaces. *Opt. Lasers Eng.* **93**, 92–99 (2017).

89. Farid, K. M. N. & Derouiche, A. *Quantifying Compartment-Specific Protein Translocation in Astrocytes by Object-Oriented Image Analysis: Mitochondrial Translocation of PKCδ. In: Di Benedetto, B. (eds) Astrocytes. Methods in Molecular Biology* **1938**, (Humana Press; New York; NY., 2019).

90. Roukos, V., Pegoraro, G., Voss, T. C. & Misteli, T. Cell cycle staging of individual cells by fluorescence microscopy. *Nat. Protoc.* **10**, 334–348 (2015).

91. Gomes, C. J., Harman, M. W., Centuori, S. M., Wolgemuth, C. W. & Martinez, J. D. Measuring DNA content in live cells by fluorescence microscopy. *Cell Div.* **13**, 1–10 (2018).

92. Schmidt, A., Mühl, M., Brito, W. A. da S., Singer, D. & Bekeschus, S. Antioxidant Defense in Primary Murine Lung Cells following Short- and Long-Term Exposure to Plastic Particles. *Antioxidants* **12**, (2023).

93. Cejas, R. B., Tamaño-Blanco, M. & Blanco, J. G. Analysis of the intracellular traffic of IgG in the context of Down syndrome (trisomy 21). *Sci. Rep.* **11**, 1–12 (2021).

94. Lu, Y. & Xu, J. Phytohormones in microalgae: A new opportunity for microalgal biotechnology? *Trends Plant Sci.* **20**, 273–282 (2015).

95. Riaz, A. *et al.* Molecular Regulation and Evolution of Redox Homeostasis in Photosynthetic Machinery. *Antioxidants* **11**, (2022).

96. Ljosa, V. *et al.* Comparison of Methods for Image- Based Profiling of Cellular Morphological Responses to Small-Molecule Treatment. *SLAS-DISCOVERY* **18**, 1321–1329 (2013).

97. Feng, Y., Mitchison, T. J., Bender, A., Young, D. W. & Tallarico, J. A. Multi-parameter phenotypic profiling: Using cellular effects to characterize small-molecule compounds. *Nat. Rev. Drug Discov.* **8**, 567–578 (2009).

98. Suzuki, S., Yamaguchi, H., Nakajima, N. & Kawachi, M. Raphidocelis subcapitata (=Pseudokirchneriella subcapitata) provides an insight into genome evolution and environmental adaptations in the Sphaeropleales. *Sci. Rep.* **8**, 1–13 (2018).

99. Blainey, P., Krzywinski, M. & Altman, N. Points of significance: Replication. *Nat. Methods* **11**, 879–880 (2014).

100. Curtis, B. J. *et al.* Cross-species transcriptomic signatures identify mechanisms related to species sensitivity and common responses to nanomaterials. *Nat. Nanotechnol.* **17**, 661–669 (2022).

101. Ostovich, E. *et al.* Physiological Impacts on Raphidocelis subcapitata in Response to Lithiated Cobalt Oxide Nanomaterials. **00**, 1–12 (2023).

102. Al-Khazali, Z. K. M. & Alghanmi, H. A. Environmental Toxicity of Nano Iron Oxides (Fe2O3 NPs) on Algal Growth Klisinema persicum and Cellular DNA Damage Using Comet Assay. *Egypt. J. Aquat. Biol. Fish.* **27**, 431–453 (2023).

103. Mesquita, D. P. P., Gomes, J. P. P., Souza Junior, A. H. & Nobre, J. S. Euclidean distance estimation in incomplete datasets. *Neurocomputing* **248**, 11–18 (2017).

104. Zhang, H. *et al.* High throughput analysis of leaf chlorophyll content in sorghum using RGB, hyperspectral, and fluorescence imaging and sensor fusion. *Plant Methods* **18**, 1–17 (2022).

105. Maxwell, K. & Johnson, G. N. Chlorophyll fluorescence - A practical guide. *J. Exp. Bot.* **51**, 659–668 (2000).

106. Weis, E. & Berry, J. A. Quantum efficiency of Photosystem II in relation to ’energy’-dependent quenching of chlorophyll fluorescence. *BBA - Bioenerg.* **894**, 198–208 (1987).

107. Ghotbi-Ravandi, A. A., Sedighi, M., Aghaei, K. & Mohtadi, A. Differential Changes in D1 Protein Content and Quantum Yield of Wild and Cultivated Barley Genotypes Caused by

Moderate and Severe Drought Stress in Relation to Oxidative Stress. *Plant Mol. Biol. Report.* (2021). doi:10.1007/s11105-020-01264-5

108. Schuurmans, R. M., Van Alphen, P., Schuurmans, J. M., Matthijs, H. C. P. & Hellingwerf, K. J. Comparison of the photosynthetic yield of cyanobacteria and green algae: Different methods give different answers. *PLoS One* **10**, 1–17 (2015).

109. Young, E. B. & Beardall, J. Photosynthetic function in Dunaliella tertiolecta (Chlorophyta) during a nitrogen starvation and recovery cycle. *J. Phycol.* **39**, 897–905 (2003).

110. Janka, E., Körner, O., Rosenqvist, E. & Ottosen, C. O. Using the quantum yields of photosystem II and the rate of net photosynthesis to monitor high irradiance and temperature stress in chrysanthemum (Dendranthema grandiflora). *Plant Physiol. Biochem.* **90**, 14–22 (2015).

111. Kale, R. *et al.* Amino acid oxidation of the D1 and D2 proteins by oxygen radicals during photoinhibition of Photosystem II. *Proc. Natl. Acad. Sci. U. S. A.* **114**, 2988–2993 (2017).

112. Yee, M. & Bartholomew, J. C. Effects of 3-(3,4-Dichlorophenyl)-1,1-Dimethylurea on the Cell Cycle in Euglena gracilis'. 1025–1029 (1989).

113. OECD. OECD Test No. 227: Terrestrial Plant Test: Vegetative Vigour Test. *OECD* 1–16 (2003). doi:10.1787/9789264076273-en

114. Yang, J., Song, Z., Ma, J., Han, H. & Han, H. Toxicity of Molybdenum-Based Nanomaterials on the Soybean-Rhizobia Symbiotic System: Implications for Nutrition. *ACS Appl. Nano Mater.* **3**, 5773–5782 (2020).

115. Majumdar, S. *et al.* Proteomic, gene and metabolite characterization reveal the uptake and

toxicity mechanisms of cadmium sulfide quantum dots in soybean plants. *Environ. Sci. Nano* **6**, 3010–3026 (2019).

116. Chen, X. B. *et al.* Hydrogen peroxide-induced chlorophyll a bleaching in the cytochrome b 6f complex: A simple and effective assay for stability of the complex in detergent solutions. *Photosynth. Res.* **90**, 205–214 (2006).

117. Battaglino, B., Grinzato, A. & Pagliano, C. Binding properties of photosynthetic herbicides with the qb site of the d1 protein in plant photosystem ii: A combined functional and molecular docking study. *Plants* **10**, 1–15 (2021).

118. Vítová, M. *et al.* Chlamydomonas reinhardtii: duration of its cell cycle and phases at growth rates aVected by temperature. *Planta* **234**, 599–608 (2011).

119. Foyer, C. H. & Noctor, G. Redox Regulation in Photosynthetic Organisms. *Regulation* **11**, 861–905 (2009).

120. Pokora, W., Aksmann, A., Baścik-Remisiewicz, A., Dettlaff-Pokora, A. & Tukaj, Z. Exogenously applied hydrogen peroxide modifies the course of the Chlamydomonas reinhardtii cell cycle. *J. Plant Physiol.* **230**, 61–72 (2018).

121. Merchant, S. S., Kropat, J., Liu, B., Shaw, J. & Warakanont, J. TAG, You're it! Chlamydomonas as a reference organism for understanding algal triacylglycerol accumulation. *Curr. Opin. Biotechnol.* **23**, 352–363 (2012).

Appendix I : Supporting Information

Chapter 1: Physiological Impacts of Raphidocelis subcapitata in Response to Lithiated Cobalt Oxide Nanomaterials.

Supplementary Table S1: LCO DSL Characterization in Algal Complete Media

[LCO]	Z-Average (d.nm)	ζ-Potential (mV)	Electrophoretic Mobility (µm·cm·Vs^{-1})
0.01 ug·mL^{-1}	334.60 ± 59.57	-2.01 ± 0.37	-0.16 ± 0.03
0.1 ug·mL^{-1}	253.10 ± 28.98	-10.07 ± 1.29	-0.79 ± 0.10
1 ug·mL^{-1}	249.87 ± 11.86	-22.73 ± 1.73	-1.78 ± 0.14
10 ug·mL^{-1}	348.83 ± 5.59	-30.33 ± 0.24	-2.38 ± 0.02

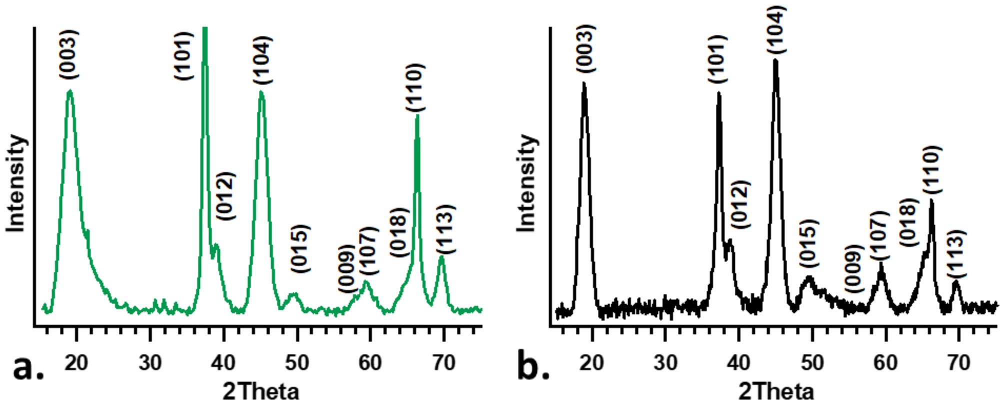

Supplementary Figure S1: (a.) XRD data from the LCO batch used in this exposure, and (b.) XRD data from a previously synthesized batch of LCO, adapted from Laudadio et al. 2018.

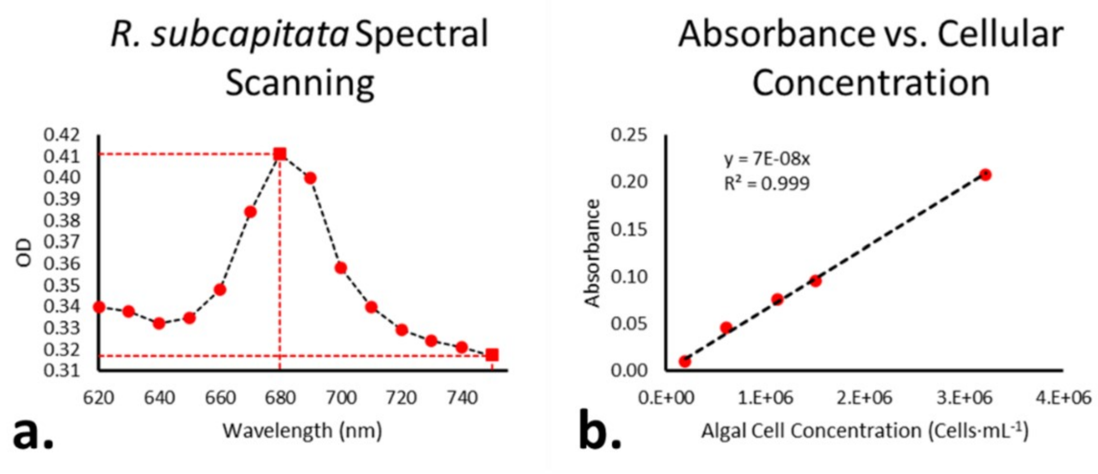

Supplementary Figure S2: (a.) Spectral scanning of *R. subcapitata*, and (b.) Cellular absorptivity at OD_{680}.

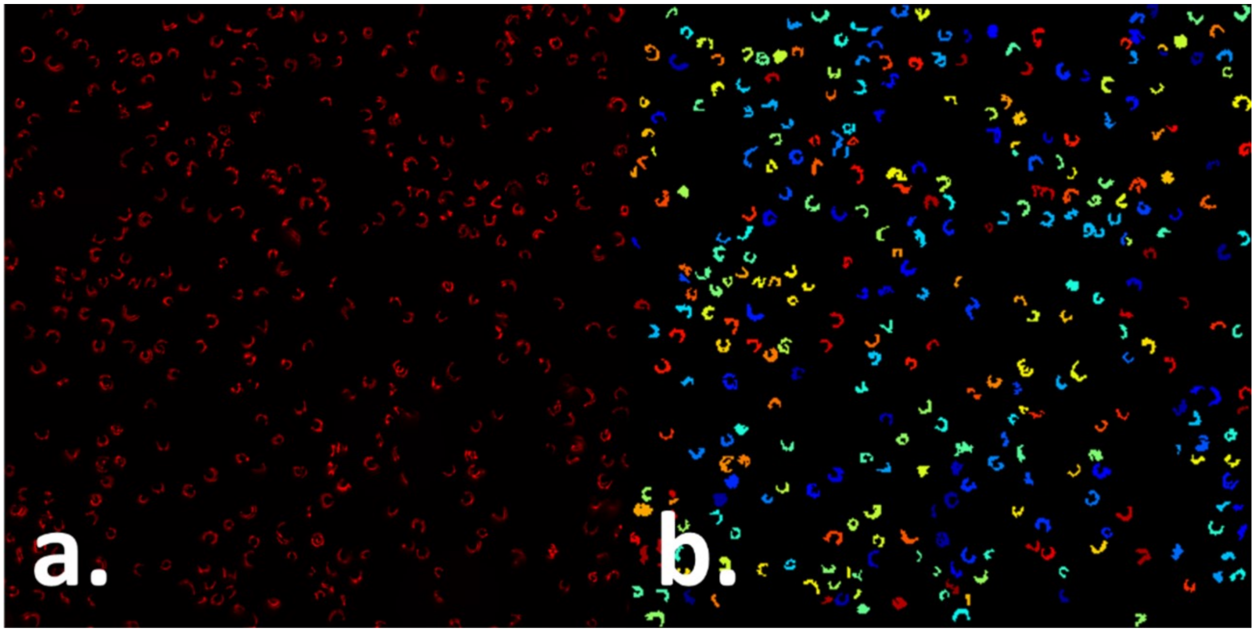

Supplementary Figure S3: (a.) Fluorescence micrograph of algal cells obtained with a 60x air objective, and (b.) subplot of corresponding image segmentation done by CellProfiler; each colored spot corresponds to a specific cell on the fluorescence micrograph.

Supplementary Table S2: VIP Scores of Reference Chemicals

Zeocin		**Carfentrazone**		**Aclonifen**		**DCMU**	
Feature	**VIP**	**Feature**	**VIP**	**Feature**	**VIP**	**Feature**	**VIP**
Mean_Cell_Chplst_AreaShape_NormalizedMoment_3_0	1.31	Mean_Cell_Mean_Masked_LDs_Number_Object_Number	1.87	Mean_Cell_Nuclei_AreaShape_Zernike_5_1	1.45	Mean_Cell_Chplst_Granularity_1_Chplst_Corrected	1.51
Mean_Cell_Chplst_AreaShape_NormalizedMoment_3_2	1.29	Mean_Cell_Mean_Masked_Chplst_Number_Object_Number	1.86	Mean_Cell_Nuclei_AreaShape_NormalizedMoment_2_2	1.45	Mean_Cell_Chplst_AreaShape_MaximumRadius	1.50
Mean_Cell_Chplst_AreaShape_NormalizedMoment_1_2	1.26	Mean_Cell_Parent_Chplsts	1.86	Mean_Cell_Nuclei_AreaShape_Extent	1.44	Mean_Cell_Chplst_AreaShape_MeanRadius	1.50
Mean_Cell_Chplst_AreaShape_SpatialMoment_1_0	1.24	Mean_Cell_Chplst_Parent_Masked_Chplst	1.86	Mean_Cell_Nuclei_AreaShape_Zernike_3_1	1.44	Mean_Cell_Chplst_AreaShape_MedianRadius	1.49
Mean_Cell_Nuclei_Granularity_3_Nuc_Corrected	1.22	Mean_Cell_LDs_Parent_Masked_LDs	1.86	Mean_Cell_Nuclei_AreaShape_HuMoment_0	1.43	Mean_Cell_Nuclei_AreaShape_Eccentricity	1.48
Mean_Cell_Chplst_Granularity_3_Chplst_Corrected	1.21	Mean_Cell_LDs_AreaShape_NormalizedMoment_2_2	1.78	Mean_Cell_Nuclei_AreaShape_Zernike_0_0	1.42	Mean_Cell_Chplst_AreaShape_Area	1.47
Mean_Cell_LDs_Granularity_6_LD_Corrected	1.21	Mean_Cell_LDs_AreaShape_NormalizedMoment_2_0	1.63	Mean_Cell_Nuclei_AreaShape_HuMoment_1	1.41	Mean_Cell_Chplst_AreaShape_CentralMoment_0_0	1.47
Mean_Cell_Mean_Masked_Nuclei_Distance_Minimum_Cell	1.21	Mean_Cell_Chplst_AreaShape_NormalizedMoment_0_3	1.63	Mean_Cell_Nuclei_AreaShape_Eccentricity	1.38	Mean_Cell_Chplst_AreaShape_SpatialMoment_0_0	1.47
Mean_Cell_Chplst_AreaShape_CentralMoment_1_2	1.21	Mean_Cell_Chplst_AreaShape_NormalizedMoment_3_0	1.63	Mean_Cell_Nuclei_AreaShape_HuMoment_2	1.37	Mean_Cell_Chplst_AreaShape_EquivalentDiameter	1.47
Mean_Cell_Mean_Masked_Chplst_Number_Object_Number	1.20	Mean_Cell_LDs_AreaShape_Extent	1.58	Mean_Cell_Nuclei_AreaShape_HuMoment_3	1.36	Mean_Cell_Nuclei_Granularity_1_Nuc_Corrected	1.46
Metolcahlor		**H_2O_2**		**Glufosinate**		**MSMA**	
Feature	**VIP**	**Feature**	**VIP**	**Feature**	**VIP**	**Feature**	**VIP**
Mean_Cell_LDs_Granularity_9_LD_Corrected	1.60	Mean_Cell_Chplst_AreaShape_NormalizedMoment_3_2	1.63	Mean_Cell_Chplst_AreaShape_Eccentricity	1.69	Mean_Cell_Chplst_AreaShape_MinorAxisLength	1.70
Mean_Cell_Nuclei_AreaShape_NormalizedMoment_3_0	1.55	Mean_Cell_Chplst_AreaShape_NormalizedMoment_1_2	1.62	Mean_Cell_Nuclei_AreaShape_CentralMoment_1_2	1.68	Mean_Cell_Chplst_AreaShape_InertiaTensorEigenvalues_1	1.67
Mean_Cell_LDs_Granularity_2_LD_Corrected	1.52	Mean_Cell_Chplst_AreaShape_NormalizedMoment_3_0	1.59	Mean_Cell_Nuclei_AreaShape_NormalizedMoment_1_2	1.67	Mean_Cell_Chplst_AreaShape_MinFeretDiameter	1.67
Mean_Cell_LDs_Granularity_7_LD_Corrected	1.52	Mean_Cell_LDs_Granularity_13_LD_Corrected	1.56	Mean_Cell_Chplst_AreaShape_MinorAxisLength	1.63	Mean_Cell_Chplst_AreaShape_Eccentricity	1.62
Mean_Cell_LDs_Granularity_6_LD_Corrected	1.50	Mean_Cell_Chplst_AreaShape_CentralMoment_1_2	1.54	Mean_Cell_Nuclei_AreaShape_NormalizedMoment_2_1	1.61	Mean_Cell_Chplst_AreaShape_NormalizedMoment_3_0	1.60
Mean_Cell_Mean_Masked_Chplst_Distance_Centroid_Cell	1.50	Mean_Cell_Chplst_Intensity_MinIntensity_Chplst_Corrected	1.53	Mean_Cell_Mean_Masked_Chplst_Number_Object_Number	1.56	Mean_Cell_Children_Masked_LDs_Count	1.57
Mean_Cell_LDs_Granularity_16_LD_Corrected	1.37	Mean_Cell_Nuclei_AreaShape_NormalizedMoment_3_0	1.51	Mean_Cell_Parent_Chplsts	1.56	Mean_Cell_Nuclei_AreaShape_CentralMoment_0_3	1.52
Mean_Cell_LDs_Granularity_8_LD_Corrected	1.37	Mean_Cell_LDs_Granularity_6_LD_Corrected	1.50	Mean_Cell_Chplst_Parent_Masked_Chplst	1.56	Mean_Cell_Chplst_AreaShape_NormalizedMoment_0_3	1.51
Mean_Cell_LDs_AreaShape_NormalizedMoment_2_0	1.35	Mean_Cell_Chplst_AreaShape_MeanRadius	1.43	Mean_Cell_Chplst_AreaShape_InertiaTensorEigenvalues_1	1.55	Mean_Cell_Nuclei_Granularity_7_Nuc_Corrected	1.50
Mean_Cell_Nuclei_AreaShape_CentralMoment_1_2	1.33	Mean_Cell_Chplst_AreaShape_MedianRadius	1.41	Mean_Cell_Chplst_AreaShape_Orientation	1.51	Mean_Cell_Chplst_AreaShape_CentralMoment_0_3	1.47

This table contains the top 10 variable importance in projection (VIP) scores for each reference chemical. VIP scores were extracted from the PLS-DA response plots of each reference chemical and indicate the unique features that are most influential in driving the separation between their response groups.

Supplementary Table S3: Interpretable Features of Biological Relevance

Treatment	**Mechanism of Action**	**Chlorophyll Content**	**Nuclei/Cell**	**TAG Content**
Ctrl	Healthy Cells	0.00	0.00	0.00
Aclonifen	Carotenoid Biosynthesis Inhibition	2.60 *	0.59	2.33
Carfentrazone	Membrane Disruption	-3.56 *	10.61 *	-1.01
DCMU	PSII Photochemistry Inhibition	-0.07	-4.74 *	-4.76 *
Glufosinate	N2 Metabolism Inhibition	2.03 *	1.98	1.29
H2O2	Oxidative Stress	-6.34 *	14.01 *	-1.93
Metolachlor	Long-Chain FA Synthesis Inhibition	0.96 *	8.36 *	9.01 *
MSMA	OP Uncouplling/ e- Transport Inhibition	0.01	0.88	-4.54 *
Zeocin	DNA Damage	1.12 *	4.93 *	1.30

This table contains the average z-scores for several biologically relevant endpoints. Here, values represent the average number of standard deviations treatment populations are above or below the mean control population. Significant differences were determined using a one-way ANOVA with a Tukey post hoc test for multiple comparisons; asterisks (*) represent significant standard deviations from the mean control population ($p<0.05$). Chlorophyll is the most important constituent of photosynthesis and changes in its levels can be used to investigate plant/algae stress.[104] Relative chlorophyll content can be analyzed through comparing the integrated intensities of chloroplast fluorescent signals. Many of the chemical treatments actually increased chlorophyll content after 24 hours at 10 μM, most notably in Aclonifen and Glufosinate treated cells. This is especially interesting for Aclonifen as its MoA is related to the inhibition of carotenoid synthesis, and has also been reported to impact chlorophyll synthesis as well.[71] However, under these specific exposure conditions, the increase in chlorophyll content may be indicative of a protective measure to compensate for initial damages/stress.[71] Conversely, H_2O_2 and Carfentrazone significantly decreased chlorophyll content under the same conditions, which does align with the literature. H_2O_2 stress, for example, has been reported to lead to the bleaching of chlorophyll.[116] The MoA of Carfentrazone is related to the inhibition of protoporphyrinogen oxidase (PPO), which promotes the accumulation of protoporphyrin IX, causing damage to the cell membrane.[41] However, PPO is also an important enzyme in the chlorophyll and heme biosynthesis pathways, and thus its inhibition coincides with lower chlorophyll.[41] Interestingly, DCMU, which most directly inhibits photosynthesis by blocking electron flow at the D1 subunit of PSII,[117] had no impact on chlorophyll content under the same conditions.

Green algae typically undergo a multiple fission reproductive pattern in which one mother cell can divide into several daughter cells, depending on the environmental cues.[67] For example, *R. subcapitata* has the ability to divide into eight daughter cells.[66] Due to this unique phenomena, measuring the number of nuclei per cell can be used to study the impact of chemicals on cell cycle progression.[24] Depending on the temperature and light intensities used to grow algae cells, the duration of the cell cycle can take anywhere between 14 & 36 hours to complete.[118] Additionally, depending on the type of stressor, impacts to cell cycle progression may also depend on the stage in which cells are exposed, as with DNA Damage.[70] Therefore, longer, and multiple, timepoints should be considered when specifically studying a chemical's impact on the cell cycle. However, comparing the average nucleation state of treated cells to that of control cells after 24 hours may be useful in obtaining an idea of whether or not a chemical has the potential to interfere with cell cycle progression. While Aclonifen and Glufosinate treatments significantly increased chlorophyll content, they did not significantly impact the nucleation state. Conversely, DCMU treated cells, on average, had significantly less nuclei/cell, compared to control cells, thus suggesting that DCMU inhibits nuclear division. This is consistent with other photosynthetic organisms, like *Euglena gracilis*, in which similar impacts have been reported.[112] On average, H_2O_2 and Carfentrazone treatments had the largest average number of nuclei per cell, which may be due to the role of reactive oxygen species (ROS) in cell signaling. For example, in algae, H_2O_2 has been reported to signal for programmed cell death, increase the number of nuclear replications within a cell cycle, and/or accelerate/delay the duration of the cell cycle progression, depending on which stage cells are exposed.[119,120] Metolachlor also significantly increased the average number of nuclei/cell, which aligns with the literature.[24] Zeocin, which causes DNA damage through promoting the double-stranded cleavage of DNA,[76] also caused a significant increase in the average number of nuclei/cell, although to a lower extent. Per the literature, this may indicate that a majority of the cells had already passed their first commitment point in the cell cycle at the time of Zeocin application, thus allowing for one round of DNA replication and nuclear division.[70]

However, if longer, and more, timepoints were measured, it is possible that that an arrest/delay in cell cycle could be observed during the second round of DNA replication/nuclear division.[70]

Green algae have the ability to accumulate large quantities of neutral lipids, namely triacylglycerol (TAG), which serve as a reservoir for energy storage.[36] However, since starch is the preferred energy storage reservoir, algae typically only produce large quantities of TAG under certain types of stressful conditions. For example, when subjected to nitrogen starvation, *Chlamydomonas reinhardtii* has been reported to significantly increase TAG content.[37] Some algae, like *R. subcapitata*, have also been reported to significantly increase TAG content under certain types of heavy meatal stress, such as nano cobalt.[101] Under the exposure conditions, most of the treatments did not elicit a significant change in TAG content. Interestingly, this includes Glufosinate, which blocks the assimilation of nitrogen through the inhibition of glutamine synthetase.[73] However, it may be possible the exposure duration was not long enough to cause nitrogen starvation. TAG content was only significantly increased in Metolachlor treated cells, which may be to due to the way it interferes with the elongation of fatty acids by inhibiting very-long-chain 3-oxoacyl-CoA synthase.[24] As a result, this may force lipid metabolism into an acyl-CoA-dependent pathway where fatty acids are converted to TAG instead of membrane lipids.[121] Conversely, MSMA and DCMU treatments significantly reduced TAG content. In both cases, this may be caused by deficiencies in intermediates, like acetyl-CoA, which are important precursors for TAG production.[36] However, more research needs to be done to address the impacts of these chemicals on lipid metabolism.

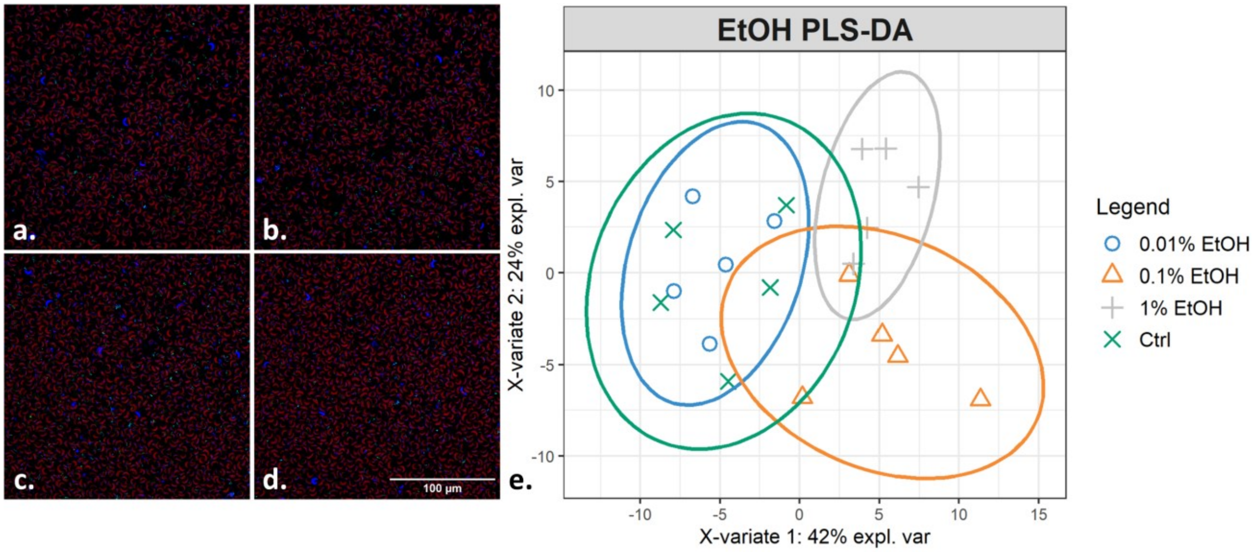

Supplementary Figure S4: Phenotypic responses to ethanol (EtOH) concentrations. A partial least squares-discriminant analysis (PLS-DA) response plot describes the change across complex morphological feature data with increasing concentration; ellipses represent 95% confidence interval.

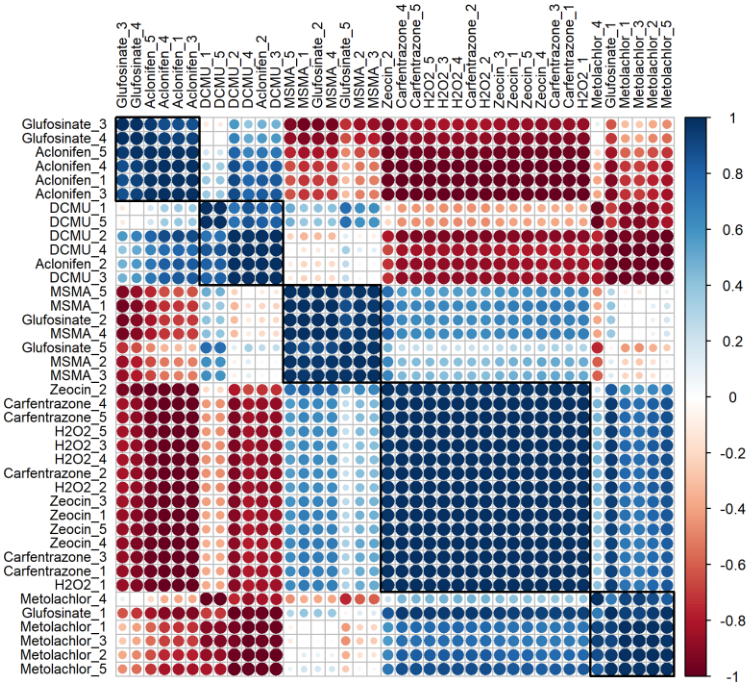

Supplementary Figure S5: Pearson correlation matrix based on minimal feature data. Chemical-treated samples are hierarchically clustered by their Pearson coefficient in relation to the other chemical-treated samples, however only based on three features of biological relevance: chlorophyll content, the number of nuclei/cell, and TAG content.